

# A Way to Picometer X-ray Displacement Sensing and Nanometer Resolution 3D X-ray Micro-Tomography

Li Hua Yu

*NSLSII, Brookhaven National Laboratory*

We introduce the two-point propagation field (TPPF)—a real-valued, phase-sensitive quantity defined as the functional derivative of the single-photon detection probability with respect to an infinitesimal opaque perturbation placed between source and detection slits. The TPPF is analytically derived and shown to exhibit stable, high-frequency sinusoidal structure ( $\approx 6.7$  nm period) near the detection slit. This structure enables shot-noise-limited displacement sensing at  $\sim 15$  pm precision using routinely available synchrotron fluxes and practical nanofabricated slit/comb geometries, requiring mechanical stability only over the final 0.5 mm. The same principle provides a foundation for future nanometer-resolution 3D X-ray micro-tomography of bulk samples with potentially reduced radiation dose. Two conceptual strategies—a central blocker and off-axis multi-slit arrays—are estimated to lower the required incident fluence by more than one order of magnitude each, yielding combined reductions of two to three orders of magnitude with near-term detector development. The TPPF concept, originally developed in a perturbative study of single-particle propagation, thus bridges fundamental quantum measurement questions with practical high-resolution X-ray metrology and imaging.

## 1. INTRODUCTION AND MOTIVATION

This technical note outlines a new theoretical concept—the two-point propagation field (TPPF)—that may offer a practical basis for achieving shot-noise-limited X-ray displacement sensing at  $\sim 15$  pm precision with existing synchrotron beamlines and practical slit-comb geometries. This approach addresses key limitations in current tomography, such as relative sample-beam motion restricting resolution to  $\sim 4$  nm [1], and is rooted in the two-point propagation field (TPPF), a real-valued, phase-sensitive function derived from perturbative analysis of single-particle propagation. TPPF is derived from the perturbative response of detection rates to localized perturbations—such as placing a thin opaque pin to block the wave—at intermediate points along the photon propagation path between a source slit and a detection slit. This quantity, referred to as the two-point propagation field (TPPF), was introduced and derived in detail in a recent theoretical study [2], where it was originally termed the "perturbative function."

The central idea is that this function captures projection-like information about a sample's internal structure by encoding how the count rate at a detector changes when the wave is perturbed by a pin at different points. When we replace the perturbation pin with a sample as the perturbation, the detection rate becomes a function of the position and the angle of the sample orientation. The function is a convolution between the TPPF and the sample's structural function. The result is a stable, reproducible function that varies with the scan position and angle of the sample, and may be viewed as analogous to the projection data used in Radon-transform-based reconstruction techniques. However, in this case, the measured signal is directly related to the Fourier transform of the Radon transform, due to the high-frequency phase information inherent in the TPPF.

Although this work does not address reconstruction techniques directly, the structure of the TPPF suggests a possible path toward extending classical tomographic methods to single-particle quantum systems—particularly in efforts to resolve nanometer-scale structural features. This note presents the TPPF formula, its physical interpretation, and a proposed connection to projection-based 3D-tomography [3, 4]. The goal is to communicate this idea clearly to researchers in 3D imaging and X-ray science, and to explore whether the method can be experimentally tested and integrated into an existing tomographic method. In the first step in this direction, the analysis leads to practical shot-noise-limited displacement sensing at  $\sim 15$  pm precision with existing synchrotron beamlines and practical slit/comb geometries. Such precision enables lensless, counting-based sensors that require stability only over the final 0.5 mm propagation distance, utilizing routine fluxes from synchrotron or XFEL sources (e.g.,  $10^{11}$  to  $10^{13}$ ) incident photons, depending on slit configurations.

This step itself is useful for the advance of x-ray tomography because the motion between the x-ray beam and the sample of order of 4 nm is one of the limitations of tomography resolution[1]. By encoding high-frequency phase information akin to a Fourier-transformed Radon projection (Section 3), the TPPF supports reconstruction of internal structures at nanometer scales, offering a pathway to lower-dose imaging compared to conventional ptychography or burst methods. This not only facilitates experimental validation of the TPPF but also reduces radiation damage in biological samples potentially by more than one order of magnitude through strategies like central blockers or off-axis slit arrays, as explored in Sections 5 and 6.

Section 2 introduces the two-point propagation function (TPPF). Section 3 examines its connection to the Radon transform and 3D tomography. In Section 4, we discuss how cascaded double or triple slit configurations can enable nanometer resolution using existing technology. In Section 5, we present the calculation of 4 practical options for a lensless picometer X-ray displacement sensor, one of our main result of this work, which bridge the TPPF testing and the further exploration of the new x-ray tomography method. Section 6 describes ongoing work for a significant reduction of the photon flux required. Section 7 discusses the relation between TPPF and the quantum measurement during the free space propagation between the source and the detector slit. Section 8 is the conclusion.

This work is approached from a theoretical standpoint, using broadly referenced parameters to assess the feasibility of a picometer x-ray displacement sensor and the nanometer-resolution 3D tomography. Although not based on direct experience with experimental tomography or biological imaging, the analysis is intended to provide a foundation for discussion and further evaluation by experts in these areas.

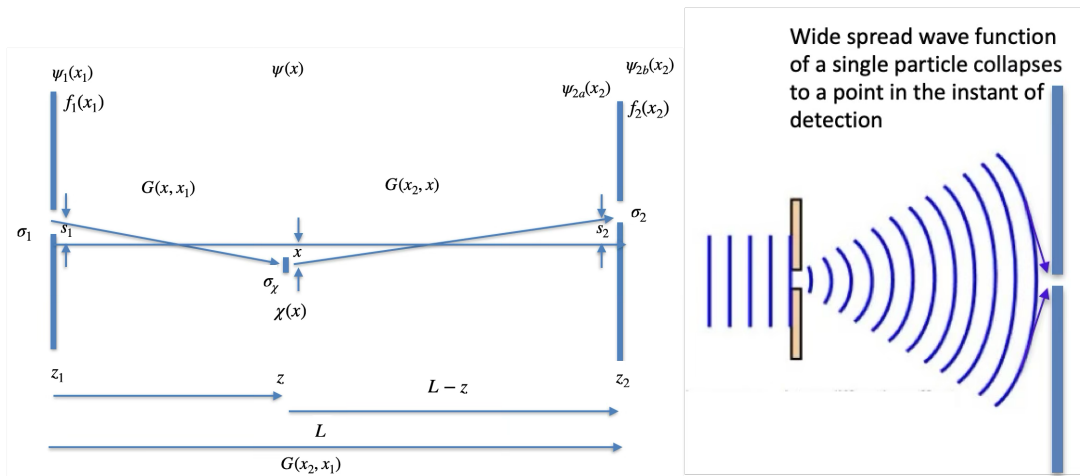


FIG. 1. (a) Experimental geometry (**not to scale**). The wave functions at slits 1,2 at  $z_1, z_2$  with apertures  $\sigma_1, \sigma_2$  and corresponding transverse displacements  $s_1, s_2$  in the  $x$ -direction, and a pin  $\chi(x)$  at  $z, x_p$  of width  $\sigma_\chi$ . The distances between the slits and the pin are  $z, L-z$ , and  $L$ . The longitudinal is the  $z$ -axis, the  $x$ -axis is vertical in this figure. The slits are perpendicular to the plane of the figure, parallel to the  $y$ -axis. We use  $\psi_1(x_1, z_1), \psi(x, z), \psi_{2a}(x_2, z_2)$  and  $\psi_{2b}(x_2, z_2)$  to represent the wave function at the entrance, the pin and the exit, respectively. The subscripts  $a$  and  $b$  represent before and after slit 2. We use  $f_1(x_1)$  and  $f_2(x_2)$  to represent the effect of the slits such that  $\psi_1(x_1, z_1) \equiv f_1(x_1), \psi_{2b}(x_2, z_2) = f_2(x_2)\psi_{2a}(x_2, z_2)$ . If we choose the slit with the hard-edged opening,  $f_1(x_1)$  and  $f_2(x_2)$  would be zero outside the slits and equal to 1 within the slits. To simplify the calculation, we assume they are Gaussian with peak value 1, except that we choose  $f_1(x_1)$  to normalize  $\psi_1$  as  $P_1 = \int dx_1 |\psi_1(x_1, z_1 = 0)|^2 = 1$ . The pin profile is  $\chi(x) = 1$  when it is removed. When inserted,  $\chi(x) = 1 - \exp(-\frac{1}{2\sigma_\chi^2} (x - x_p)^2)$ ; effective width (equivalent hard-edged slit width) is  $\Delta x = \sqrt{2\pi}\sigma_\chi$ . (b) The wave function of a single particle spreads over a wide region after emission and collapses instantaneously upon detection

## 2. DESCRIPTION OF THE EXPERIMENT TO MEASURE THE TWO-POINT PROPAGATION FIELD

### 2.1 TPPF and its physical interpretation

As illustrated in Figure 1(a), we analyze the wave function evolution of a particle when it propagates through free space in the longitudinal  $z$ -direction from a thin entrance slit 1 to a detector behind a thin exit slit 2 to find the information about whether the wave function collapse occurs at the entrance slit 1 or the exit slit 2. The slits are parallel to the  $y$ -axis (perpendicular to the plane of the figure). The  $x$ -axis is vertical in the figure. Between the slits, the wave function must follow the Schrödinger equation because the only non-unitary (irreversible) process is at the slits. Only the particles that pass through the slits are selected and detected. The probability of a particle found between  $z_1$  and  $z_2$  is a constant independent of  $z$  due to particle number conservation. We insert a thin pin  $\chi(x) = 1 + \Delta\chi(x)$  between the two slits at position  $z, x$  to cut off the wave function as a perturbation. When  $\Delta\chi(x) = 0$ , there is no pin. When  $\Delta\chi(x, z) = -1$  within a thin section  $\Delta x$  around a point at  $(x, z)$ , it represents a thin pin. When  $|\Delta\chi(x, z)| \ll 1$  in an extended area, it becomes a sample as a perturbation. The caption for Fig. 1(a) gives the notations.

In Fig.1(a), we study the effect of a perturbation  $\Delta\chi(x)$  on the counting rate  $P_{2b} = \int_{-\infty}^{\infty} dx_2 |\psi_{2b}(x_2)|^2$ , and calculate the ratio of the counting rate change over the perturbation. As the perturbation approaches zero, the ratio  $\frac{\Delta P_{2b}}{\Delta\chi(x, z)}$  becomes the functional derivative  $\frac{\delta P_{2b}}{\delta\chi(x, z)}$  of the counting rate over the perturbation  $\Delta\chi(x)$ . This perturbative function is independent of perturbation, it is a real-valued function containing high-resolution phase information, determined solely by the two-slit geometry in our 2D study, as we will show in the following. It can be measured with high precision and reproducibility, and it uniquely characterizes the individual event of a particle propagating between the two slits. Unlike a probability amplitude, it manifests as a stable, reproducible structure that we interpret as consistent with an objectively existing field, which we define as the two-point propagation field (TPPF). The TPPF does not correspond to a probability distribution. While the wave function describes an ensemble of possible detection outcomes, the TPPF characterizes the process underlying a single detection — a realization selected according to the Born rule.

In Appendix II we outline a derivation of the calculation of TPPF using the basics of quantum mechanics. Since in this work we consider X-ray 3D tomography, for the case in Fig.1 (a) and for sufficiently long and narrow slits and pin, we neglect the  $y$  dependence and assume a 2D Maxwell equation

$$\frac{1}{c^2} \frac{\partial^2}{\partial t^2} \phi(x, z, t) = \left( \frac{\partial^2}{\partial x^2} + \frac{\partial^2}{\partial z^2} \right) \phi(x, z, t), \quad (1)$$

because we do not consider polarization, we just use  $\phi$  to denote any component of the electromagnetic field. We assume  $k = \frac{\omega}{c}$ ,  $\phi(x, z, t) = e^{i(kz - \omega t)} \psi(x, z)$ , take the paraxial approximation:  $|\frac{\partial^2}{\partial z^2} \psi| \ll |\frac{\partial^2}{\partial x^2} \psi|$ ,  $|\frac{\partial^2}{\partial z^2} \psi| \ll 2k |\frac{\partial}{\partial z} \psi|$ , we get the 1D Schrödinger equation  $i \frac{\partial}{\partial z} \psi = -\frac{1}{2k} \frac{\partial^2}{\partial x^2} \psi$ .  $\psi$  is the slowly varying amplitude and phase of the wave function. We can characterize the experiment by specifying the wavelength  $\lambda = \frac{2\pi}{k}$  only. The Green's function from slit 1 to slit 2 is

$$G(x_2, x_1; z_2, z_1) = \left( \frac{k}{2\pi i(z_2 - z_1)} \right)^{\frac{1}{2}} \exp \left[ i \frac{k}{2(z_2 - z_1)} (x_2 - x_1)^2 \right] \quad (2)$$

The initial wave function  $\psi_1(x_1, z_1) \equiv f_1(x_1) = \left( \frac{1}{2\pi\sigma_1^2} \right)^{\frac{1}{4}} \exp(-\frac{1}{4\sigma_1^2}(x_1 - s_1)^2)$  is the Gaussian profile of slit 1,  $f_2 = \exp(-\frac{1}{4\sigma_2^2}(x_2 - s_2)^2)$  is for slit 2. Our analysis shows that for the narrow slits we considered, replacing the Gaussian profile by a hard-edge profile of width  $\sqrt{2\pi}\sigma_2$  would only cause a negligible difference, while the Gaussian profile allows us to derive a simple analytical result to be described in Section 2.2.

In the derivation of the TPPF, the Green's functions  $G(x, x_1), G(x_2, x)$  are given by replacing the corresponding variables in Eq.(2). When wave function at the entrance slit 1 is normalized as  $\psi_1(x_1, z_1) \equiv f_1(x_1)$ , applying the property of the Green's function, without the pin, the wave function at the exit of slit 2 is  $\psi_{2b}(x_2) = f_2(x_2) \int_{-\infty}^{\infty} dx G(x_2, x; t_2 - t) \int_{-\infty}^{\infty} dx_1 G(x, x_1; t - t_1) f_1(x_1)$ . When there is a perturbation  $\chi(x) = 1 + \Delta\chi(x)$  of a pin, the wave function after the slit 2 is

$$\psi_{2b}(x_2) + \Delta\psi_{2b}(x_2) = f_2(x_2) \int_{-\infty}^{\infty} dx G(x_2, x; t_2 - t) (1 + \Delta\chi(x)) \int_{-\infty}^{\infty} dx_1 G(x, x_1; t - t_1) f_1(x_1) \quad (3)$$

The increment for infinitesimal  $\Delta x$  is

$$\begin{aligned} \Delta\psi_{2b}(x_2) &= f_2(x_2) \int_{-\infty}^{\infty} dx G(x_2, x; t_2 - t) \Delta\chi(x) \int_{-\infty}^{\infty} dx_1 G(x, x_1; t - t_1) f_1(x_1) \\ &= - \int_x^{x+\Delta x} dx f_2(x_2) G(x_2, x; t_2 - t) \int_{-\infty}^{\infty} dx_1 G(x, x_1; t - t_1) f_1(x_1) \\ &= -\Delta x f_2(x_2) G(x_2, x; t_2 - t) \int_{-\infty}^{\infty} dx_1 G(x, x_1; t - t_1) f_1(x_1) \end{aligned}$$

Thus the functional derivaive of  $\psi_{2b}(x_2)$  over the perturbation is

$$\frac{\delta\psi_{2b}(x_2)}{\delta\chi(x, z)} = \frac{\Delta\psi_{2b}(x_2)}{\Delta x} = -f_2(x_2) G(x_2, x; t_2 - t) \int_{-\infty}^{\infty} dx_1 G(x, x_1; t - t_1) f_1(x_1) \quad (4)$$

The TPPF is the functional derivative of the detection probability  $P_{2b} = \int_{-\infty}^{\infty} dx_2 |\psi_{2b}(x_2)|^2$  over the perturbation  $\Delta\chi(x)$ , and we define the complex part of TPPF as  $\frac{\delta P_{2b}^{(c)}}{\delta\chi(x,z)} \equiv \int_{-\infty}^{\infty} dx_2 \frac{\delta\psi_{2b}(x_2)}{\delta\chi(x,z)} \psi_{2b}^*(x_2)$ , we have,

$$\frac{\delta P_{2b}}{\delta\chi(x,z)} = \int_{-\infty}^{\infty} dx_2 \frac{\delta\psi_{2b}(x_2)}{\delta\chi(x,z)} \psi_{2b}^*(x_2) + \int_{-\infty}^{\infty} dx_2 \psi_{2b}(x_2) \frac{\delta\psi_{2b}^*(x_2)}{\delta\chi(x,z)} \equiv \frac{\delta P_{2b}^{(c)}}{\delta\chi(x,z)} + c.c. \quad (5)$$

Applying Eq.(4) , we have the complex TPPF

$$\begin{aligned} \frac{\delta P_{2b}^{(c)}}{\delta\chi(x,z)} &= - \int_{-\infty}^{\infty} dx_2 \int_{-\infty}^{\infty} dx_1 \psi_{2b}^*(x_2) f_2(x_2) G(x_2, x; t_2 - t) G(x, x_1; t - t_1) f_1(x_1) \\ &= \int_{-\infty}^{\infty} dx_2 f_2^2(x_2) G(x_2, x; t_2 - t) \int_{-\infty}^{\infty} dx_1 G(x - x_1, x_1; t - t_1) f_1(x_1) \int_{-\infty}^{\infty} dx_1' G^*(x_2 - x_1'; t_2 - t_1) f_1(x_1') \end{aligned} \quad (6)$$

The last step shows there is a simple relation between TPPF and the probability  $P_{2b}$ , i.e.

$$\begin{aligned} \int_{-\infty}^{\infty} dx \frac{\delta P_{2b}^{(c)}}{\delta\chi(x,z)} &= \int_{-\infty}^{\infty} dx_2 f_2^2(x_2) \left( \int_{-\infty}^{\infty} dx G(x_2, x; t_2 - t) \int_{-\infty}^{\infty} dx_1 G(x - x_1, x_1; t - t_1) f_1(x_1) \right) \psi_{2a}^*(x_2) \\ &= \int_{-\infty}^{\infty} dx_2 f_2^2(x_2) \psi_{2a}(x_2) \psi_{2a}^*(x_2) = \int_{-\infty}^{\infty} dx_2 \psi_{2b}(x_2) \psi_{2b}^*(x_2) = P_{2b} \\ P_{2b} &= \frac{1}{2} \int_{-\infty}^{\infty} dx \frac{\delta P_{2b}^{(c)}}{\delta\chi(x,z)} + c.c. = \frac{1}{2} \int_{-\infty}^{\infty} dx \frac{\delta P_{2b}}{\delta\chi(x,z)} \end{aligned} \quad (7)$$

Thus, the integration of TPPF over  $x$  is not the probability but twice of it. An important observation is that  $\frac{1}{2P_{2b}} \frac{\delta P_{2b}}{\delta\chi(x,z)}$  is a function of  $z$ , i.e. the position  $z$  of the pin, but  $\frac{1}{2P_{2b}} \int_{-\infty}^{\infty} dx \frac{\delta P_{2b}}{\delta\chi(x,z)} = 1$  is independent of  $z$  and represents the particle number conservation during the free propagation in free space. Although the two-point propagation field (TPPF) is not positive-definite, its integral over space yields a conserved total probability. When normalized and scaled by  $h\nu$ , it acquires the dimensions of energy density and integrates to the particle's total energy. The possibility of local negative values is not without precedent; similar behavior occurs in quantum field theory, such as in the Casimir effect [6]. We therefore interpret the scaled TPPF as a generalized energy density associated with the spatial structure of single-particle propagation.

Since  $\frac{1}{2P_{2b}} \frac{\delta P_{2b}}{\delta\chi(x,z)}$  is the real part of the complex-valued  $\frac{\delta P_{2b}^{(c)}}{\delta\chi(x,z)}$ , its imaginary part—and thus the full complex derivative—can be readily obtained via a Hilbert transform[7] by multiplying the coefficients of the Fourier transform of  $\frac{1}{2P_{2b}} \frac{\delta P_{2b}}{\delta\chi(x,z)}$  by a constant according to the sign of the frequency of the term (see Appendix A) and followed by an inverse Fourier transform. As we shall show,  $\psi(x, z)$  and  $\frac{1}{2P_{2b}} \frac{\delta P_{2b}}{\delta\chi(x,z)}$  are entirely different functions:  $\psi(x, z)$  is wide spread as illustrated in Fig.1(b), however  $\frac{1}{2P_{2b}} \frac{\delta P_{2b}}{\delta\chi(x,z)}$  becomes wide spread only in between the two slits and finally converges into the slit 2. This answered the fundamental question: the evolution of the energy distribution  $h\nu$  is continuous without sudden collapse at the detector, as suggested by the TPPF model, even though the wave function  $\psi(x)$  collapses at the instant of the detection.  $\psi(x)$  represents a statistical distribution of the ensemble, while  $\frac{1}{2P_{2b}} \frac{\delta P_{2b}}{\delta\chi(x,z)}$  represents an individual realization of the ensemble.

## 2.2 The Expression of TPPF and its Difference from the Wave Function $\psi(x)$

This simple relation between TPPF and counting rate in Eq.(7) is used in simplifying the derivation of the complex TPPF Eq.(6) in Appendix II. The result for the counting rate (i.e., the probability)  $P_{2b}$  and the explicit complex valued TPPF  $\frac{\delta P_{2b}^{(c)}}{\delta \chi(x,z)}$  is simpler when expressed in terms of a few scaled parameters for slits width, and longitudinal position:  $\mu \equiv \frac{4\pi\sigma_1^2}{\lambda L} = \frac{2k\sigma_1^2}{L}$ ,  $\rho \equiv \frac{\sigma_2^2}{\sigma_1^2}$ ,  $z_2 = L, z_1 = 0, z = \xi L$ :

$$\begin{aligned} P_{2b} &= \sqrt{\frac{\mu^2 \rho}{\mu^2 + \rho\mu^2 + 1}} \exp\left(-\frac{1}{2\sigma_1^2} \frac{\mu^2}{\mu^2 + 1 + \mu^2\rho} (s_1 - s_2)^2\right) \\ \frac{\delta P_{2b}^{(c)}}{\delta \chi(x,z)} &= P_{2b} \frac{\sqrt{-\alpha_\chi}}{\sqrt{\pi}} \exp\left(\alpha_\chi (x - x_c)^2\right) \\ \alpha_\chi &= -\frac{1}{2\sigma_1^2} \frac{i\mu(\mu^2 + \rho\mu^2 + 1)}{(-i\mu + \xi)(\mu(i\xi - \mu)\rho + 2(\xi - 1)(i\mu + 1))} \end{aligned} \quad (8)$$

Here  $x_c = \frac{c_{S1}s_1 + c_{S2}s_2}{\mu^2 + \rho\mu^2 + 1}$ ,  $s_1, s_2$  are the transverse displacement of the slits in Fig.1(a), and  $c_{S1} \equiv \rho\mu^2 - (i\mu + 1)(\xi - 1)$ ,  $c_{S2} \equiv (\mu - i)(\mu + i\xi)$ . For the next discussion on the tomography, we only consider the case of  $s_1 = s_2 = 0$ , thus  $x_c = 0$ , and hence TPPF is characterized mainly by the probability  $P_{2b}$  and  $\alpha_\chi$  that provides the information about the distribution width, fringe spacing, and frequency bandwidth. etc. of TPPF.

In the example in Fig.2(a), we display the TPPF using a color scale for a case of  $\lambda = 0.541\text{nm}$  with the setup parameters in Fig.1. The red contour in Fig.2(a) is also plotted as the contour of main peak for the case of  $s_2 = 50\mu\text{m}$  in Fig.3, where we show several different contours of the main peaks for  $s_2 = 0, 25, 50, 75\mu\text{m}$  respectively, to show the different realizations of the ensemble represented by the Schrödinger equation solution, the wave function  $\psi(x)$  with initial condition  $\psi_1(x_1, z_1) \equiv f_1(x_1)$ .

Fig.2 (b,c,d) shows several regions in Fig.2(a) near the exit slit 2 with details important for the next micro-tomography discussion. In particular, Fig.2(b) shows that the evolution of the TPPF is continuous from  $z = 0.498\text{m}$  to  $Z = 0.5\text{m}$  at the exit.

To compare TPPF with  $\psi(x)$ , the RMS of  $|\psi(x,z)|^2$  is shown in Fig.3, as the thick dashed cyan line, showing its width continues to spread till the exit screen. Fig.3 shows the contours of TPPF's central peak emitted from slit 1 with the shape of a spindle projected in different directions; their width increases to a maximum in the middle at about 0.25m from the end at 0.5 m. The width of the central peak decreases after the maximum and finally, without a lens or focusing device, converges into the end slits. When the slit 2 is much narrower than the slit 1, as for the case of Fig.2, the two sides of the central peaks are wave packets with increasing width like the the width of  $\psi(x)$  until very close to the exit slit 2 within a few hundreds  $\mu\text{m}$ , where they converge rapidly into the slit 2 as shown in Fig.2(b) and Fig.2(c).

The rapid convergence is evident in Fig.2(b); in particular, comparing the horizontal and vertical scales reveals that the convergence angle is much larger than the apparent 90 degrees—despite the fact that this is free-space propagation without any focusing. This phenomenon has a profound meaning for the photon wave packet propagation: the existence of the exit slit allowing the wave packet with energy  $h\nu$  to pass through has a profound influence on the rapid convergence into the exit before it reaches the slit. In the analysis of the 1D Schrödinger equation  $i \frac{\partial}{\partial z} \psi = -\frac{1}{2k} \frac{\partial^2}{\partial x^2} \psi$ , we use the transformation  $\phi(x, z, t) = e^{i(kz - \omega t)} \psi(x, z)$ , to study only monochromatic photons. When we introduce energy bandwidth, and hence study the pulse structure of the wave packet, we would be able to analyze the time-dependent behavior of the photon wave packet and further explore how the exit slit influences the convergence process. This would be an important issue to be studied.

The distribution of different wave packets is described by  $\psi(x, z)$  as illustrated in Fig.1(b). The comparison of Fig.1(b) and Fig.3 clearly shows  $\psi(x, z)$  more like a water wavefront propagating in a pond while the different wave packets  $\frac{\delta P_{2b}^{(c)}}{\delta \chi(x,z)}$  of various  $s_2$  are more like projectiles with detailed phase information as visible fringes in Fig.2(a) shooting into

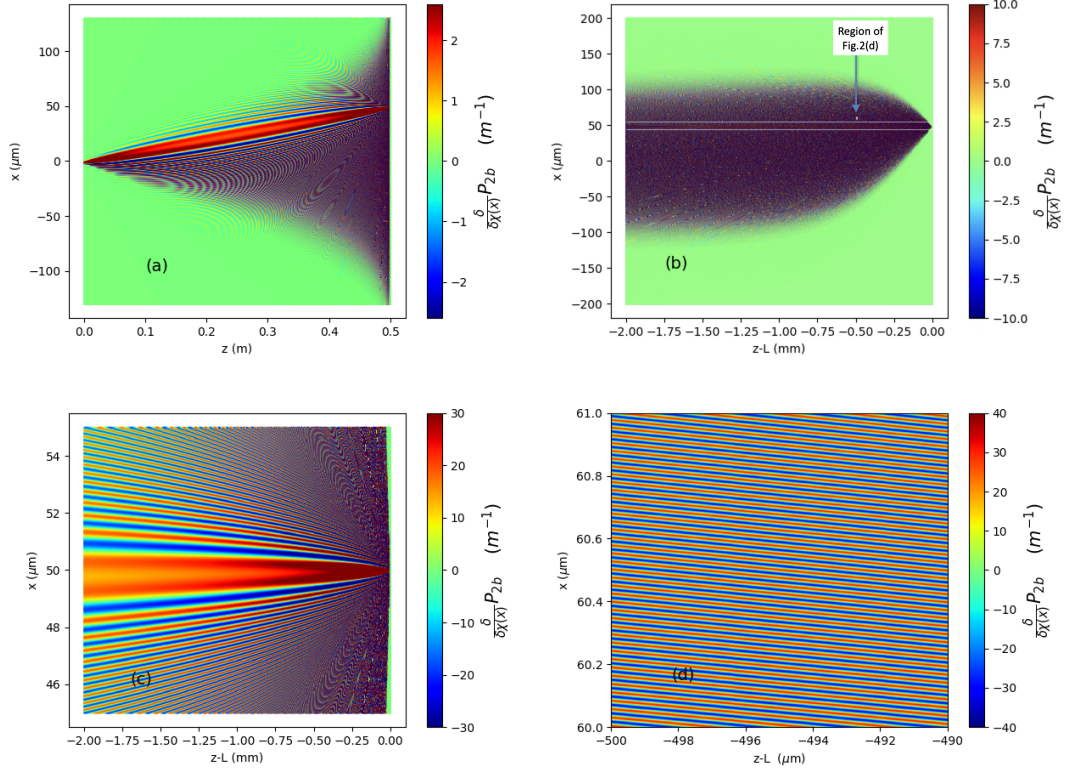


FIG. 2. For a setup in Fig.1(a), take  $\lambda = 0.541nm$ ,  $\sigma_2 = 0.8nm$ ,  $\sigma_1 = 0.5\mu m$ ,  $L = 0.5m$ ,  $L - z = 0.5mm$ , Fig.2(a):  $\frac{\delta P_{2b}}{\delta \chi(x,z)}$  vs.  $x, z$  in color scale for  $s_2 = 50\mu m$ ,  $P_{2b} = 9.47 \times 10^{-6}$ . Some elliptical patterns are artifact due to the limited number of points of the plot and the nearly periodic structure of the function  $\frac{\delta P_{2b}}{\delta \chi(x,z)}$ . The patterns change with the number of points of the plot, but it is hard to avoid even with pixels increased to  $4 \times 10^6$  in the plot. Fig.2(b): A narrow region within 2mm from the slit 2 in (a) showing the details not visible in (a). The detailed fringe structure is not visible in this plot because it is visible only when magnified, as given in the following (c) and (d) plots. The region between the two white lines ( $45\mu m < x < 55\mu m$ ) is given in (c) with details. The hardly visible white dot, which is too small to be recognized as a box, indicates the region (pointed to by the arrow in Fig.2(b)) shown in (d) with fringe details. Fig.2(c): The region ( $45\mu m < x < 55\mu m$ ) indicated by the two white lines in (b). Fig.2(d): The region indicated in (b) by an arrow as a white dot in a box size of  $10\mu m \times 1\mu m$  ( $60\mu m < x < 61\mu m$ ,  $-500 < z - L < -490\mu m$ ) shows the fringe structure. The most pronounced feature is that the amplitude ( $\pm 30m^{-1}$ ) indicated by the color scale is comparable to the peak amplitude in Fig.2(c).

different directions in Fig.3. This observation leads to the conclusion that  $\psi(x)$  represents a statistical distribution of the ensemble, while  $\frac{1}{2P_{2b}} \frac{\delta P_{2b}}{\delta \chi(x,z)}$  represents an individual realization of the ensemble. The main point is that the evolution of TPDF in Fig.2(b) further clarified the answer to a fundamental question to be addressed later in Section 7: we understand that it represents a continuous evolution of the energy distribution  $h\nu$ , unlike the sudden discontinuous collapse of the probability amplitude  $\psi(x, z)$  at the exit slit.

### 2.3 Explore Possible Application to Microscopy, Envelope width $\sigma_w$ , First phase $\pi$ shift fringe spacing $x_\pi$ , and number of fringes $n_f$ within $\sigma_w$ .

Further examine the details of Fig. 2(a) indicates the high resolution fine fringes with significant amplitude become hardly visible near the end slit 2 because when the width becomes close to the narrow slit size  $\sigma_2$ , the fringe spacing becomes too narrow to be visible and needs a detailed plot. Fig.2(d) shows that even at  $60\mu m$ , i.e.,  $10\mu m$  away from the centroid  $x_{c0} = 50\mu m$ , the amplitude of  $\frac{\delta P_{2b}}{\delta \chi(x,z)}$  oscillation is still at  $\pm 30m^{-1}$ , almost the same as the peak value at  $x_{c0}$ . These details hint at a possible application of TPDF in microscopy. To explore further, we consider the x-ray wavelength at  $\lambda = 0.541nm$ , and apply Eq.(8) to a finite pin width of 3 nm. The relative counting rate is a convolution

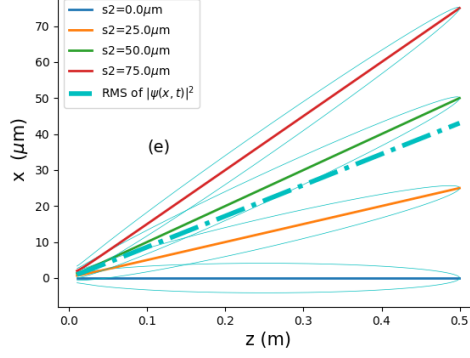


FIG. 3. The contours of  $\frac{\delta P}{\delta \chi(x,z)}$ . The colored lines are the centroids  $x_{c0}$  for  $s_2 = 0, 25, 50, 75 \mu\text{m}$ , respectively. The cyan colored contours  $x_{c0} \pm \frac{1}{2}x_\pi$  represent the contours of the main peaks of TPPF for various  $s_2$ .  $x_\pi$  here is the distance from the centroid  $x_{c0}$  to the point with phase shift from the centroid  $x_{c0}$  by  $\pi$ . For  $s_2 = 50 \mu\text{m}$ , this contour corresponds to the red colored region in Fig.2(a). As a comparison, the RMS of the wave function  $|\psi(x,t)|^2$  is the thick dashed cyan line showing its width continues to spread till the end.

of the TPPF with the pin with a Gaussian profile  $\Delta\chi(x-x_p) = -\exp(-\frac{1}{2\sigma_\chi^2}(x-x_p)^2)$ . Since TPPF is the functional derivative of the counting rate  $P_{2b}$  with respect to the perturbation  $\Delta\chi(x-x_p)$ , we have the counting rate change as

$$\frac{\Delta P_{2b}(x)}{P_{2b}} = \frac{1}{P_{2b}} \int \frac{\delta P_{2b}}{\delta \chi(x_p, z)} \Delta\chi(x-x_p) dx_p = - \left( \frac{-2\alpha_\chi \sigma_\chi^2}{1-2\alpha_\chi \sigma_\chi^2} \right)^{\frac{1}{2}} \exp\left( \frac{\alpha_\chi x^2}{1-2\alpha_\chi \sigma_\chi^2} \right) + c.c. \quad (9)$$

When the pin is sufficiently narrow, it is equivalent to a hard-edged pin of width  $\sqrt{2\pi}\sigma_\chi = 3\text{nm}$  in this case. Since  $\frac{\delta P_{2b}}{\delta \chi(x,z)}$  and  $\Delta\chi(x-x_p)$  are Gaussian, the integral is Gaussian.

For Fig. 4, the parameters in Fig. 1(a) are  $\sigma_2 = 0.8\text{nm}$ ,  $\sigma_1 = 0.5\mu\text{m}$ ,  $L = 0.5\text{m}$ ,  $\sqrt{2\pi}\sigma_\chi = 3\text{nm}$ , we choose  $L-z = 0.5\text{mm}$ , i.e., the plot is the  $x$  profile of  $-\frac{\Delta P_{2b}(x_p)}{P_{2b}}$  at  $0.5\text{mm}$  from the detector slit 2. When the pin blocks the wave function,  $\Delta P_{2b}(x_p) < 0$ , the counting rate drops. Since we only limit to the case of  $s_1 = s_2 = 0$ ,  $x_c = 0$ , we have  $\frac{\delta P_{2b}}{\delta \chi(x,z)} = P_{2b} \frac{\sqrt{-\alpha_\chi}}{\sqrt{\pi}} \exp(\alpha_\chi x^2) + c.c.$ , and  $x_{c0} = 0$ . TPPF is simpler, and determined by the main parameter  $\alpha_\chi$ , its amplitude and phase dominated by the factor  $\exp(\alpha_{\chi r} x^2) = \exp(\alpha_{\chi r} x^2) \exp(i\alpha_{\chi i} x^2)$ . In general, we are interested in a region in Fig.1 very close to slit 2, such that  $\mu, \rho, \xi \ll 1$ . For the example in Fig. 4,  $\mu \equiv \frac{4\pi\sigma_1^2}{\lambda L} = \frac{4\pi \times (0.5\mu\text{m})^2}{0.541\text{nm} \times 0.5\text{m}} = 0.0116$ ,  $\rho \equiv \frac{\sigma_2^2}{\sigma_1^2} = \left( \frac{0.8\text{nm}}{0.5\mu\text{m}} \right)^2 = 2.56 \times 10^{-6}$ ,  $z_2 = L$ ,  $z_1 = 0$ ,  $1-\xi = \frac{L-z}{L} = \frac{0.5\text{mm}}{0.5\text{m}} = 10^{-3}$  (see Section 2.2). The approximation of  $\alpha_{\chi r}, \alpha_{\chi i}$  given in Appendix III shows  $\alpha_\chi = \alpha_{\chi r} + i\alpha_{\chi i}$  is a complex-valued parameter

$$\begin{aligned} \alpha_{\chi i} &\approx \frac{\pi}{\lambda L} \frac{1}{1-\xi} \approx \frac{\pi \times 1000}{0.541\text{nm} \times 0.5\text{m}} \approx 11.6 \times 10^{12} \text{m}^{-2} \\ \alpha_{\chi r} &\approx - \left( \frac{\pi}{\lambda L} 2\sigma_1 \right)^2 \left( 1 + \frac{\rho}{2(\xi-1)^2} \right) \approx - \left( \frac{2\pi \times 0.5 \times 10^{-6} \text{m}}{0.541\text{nm} \times 0.5\text{m}} \right) \left( 1 + \frac{2.56 \times 10^{-6}}{2 \times 10^{-6}} \right) \approx -3.07 \times 10^8 \text{m}^{-2} \end{aligned} \quad (10)$$

This is simple and easy for back-of-the-envelope estimation with negligible errors. The factor  $\exp(i\alpha_{\chi i} x^2)$  with  $|\alpha_{\chi i}| \gg |\alpha_{\chi r}|$  and  $\alpha_{\chi r} < 0$ , shows TPPF in Eq.(8) gives a wave with high spatial frequency  $k_x = 2\alpha_{\chi i} x$  chirped

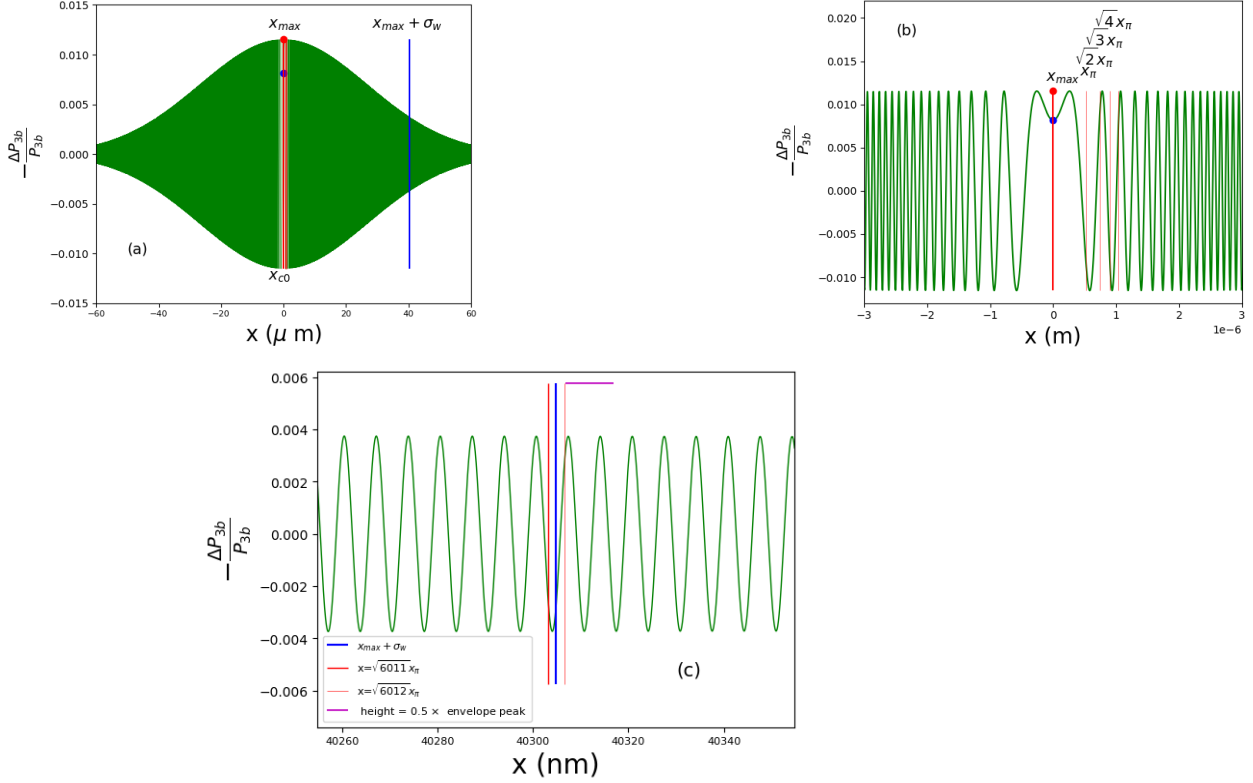


FIG. 4.  $\lambda = 0.541\text{nm}$ ,  $\sigma_2 = 0.8\text{nm}$ ,  $\sigma_1 = 0.5\mu$ ,  $L = 0.5\text{m}$ ,  $z_1 - z = 0.5\text{mm}$ ,  $\Delta\chi\Delta x = 3\text{nm}$  (a) around peak at  $|x| < 60\mu\text{m}$ . (b) around peak at  $|x| < 3\mu\text{m}$ . (c) in region around  $x = x_{max} + \sigma_w$ ,  $x_\pi = 0.52\mu\text{m}$ ,  $\sqrt{6012}x_\pi - \sqrt{6011}x_\pi = 3.35\text{nm}$ ,  $\sigma_w \approx 40\mu\text{m}$ .  $P_{2b} = 1.86 \times 10^{-5}$  for this configuration.

linearly increasing with  $x$ , while the amplitude factor  $\exp(\alpha_{\chi r}x^2)$  gives a slow exponential drop with increasing  $x$ , and reaches the beam waist at  $\sigma_w \equiv \sqrt{-\frac{1}{2\alpha_{\chi r}}} \approx \sqrt{\frac{1}{2 \times 3.07 \times 10^8 \text{m}^{-2}}} \approx 40\mu\text{m}$  determined by  $\exp(\alpha_{\chi r}\sigma_w^2) = \exp(-0.5) \approx 0.6$ .

Fig.4(a) shows around the center at  $x = x_{c0} = 0$ , where  $x_{c0}$  is defined as the point of the stationary phase, the solution of  $\frac{\partial}{\partial x} \text{Im}(\alpha_\chi(x - x_c)^2) = 0$ . The phase is stationary at the origin, the phase advance increases as  $x$ , the frequency increases linearly with  $x$ , and reaches such a high frequency in only a few  $\mu\text{m}$  that we can see only the envelope determined by absolute value  $|P_{2b} \frac{\sqrt{-\alpha_\chi}}{\sqrt{\pi}} \exp(\alpha_\chi x^2)|$ . Its width  $\sigma_w \approx 40\mu\text{m}$  is indicated by the blue lines in Fig.4(a).

More details at the central peak are shown in Fig. 4(b), where we see that the phase of the stationary point  $x_{c0}$  is not zero. The red lines indicates the points where the phase shift is  $\pi, 2\pi, \dots, 4\pi, \dots$ , their spacing is not uniform, they are located at distance from  $x_{c0}$  by  $x_\pi, \sqrt{2}x_\pi, \sqrt{3}x_\pi, \sqrt{4}x_\pi, \dots, \sqrt{n_f}x_\pi, \dots$ , where  $x_\pi = \sqrt{\frac{\pi}{\alpha_{\chi i}}} = 0.52\mu\text{m}$ . Thus, the fringe spacing becomes much narrower at the width of  $x = \sigma_w$ .

Fig.4(c) shows the fringes at the envelope width  $\sigma_w$ , where the blue line indicates the position at the width  $\sigma_w \approx 40\mu\text{m}$ , the two red lines indicate the spacing between two points of index  $n_f = 10473$  and  $n_f = 10474$  is  $(\sqrt{n_f + 1} - \sqrt{n_f})x_\pi = \sqrt{6012}x_\pi - \sqrt{6011}x_\pi = 3.35\text{nm}$ . The number of fringes within the width  $\sigma_w$  is  $n_f = \frac{\sigma_w^2}{x_\pi^2} \approx 6011$ , the fringes are so densely packed that Fig.4(a) can only show the envelope of  $\frac{\Delta P_{2b}(x)}{P_{2b}}$  while the amplitude only drops from 0.0115 to 0.003 for  $\sqrt{2\pi}\sigma_\chi = 3\text{nm}$ . If the pin is much thinner than 3nm, which is nearly half the period in this case, at  $x = \sigma_w$ , the amplitude is  $\exp(-\alpha_{\chi r}\sigma_w^2) \approx 0.6$  of the peak. The frequency of the waveform in a small range of Fig.4(c) is almost constant like a sinusoidal wave, while from the centroid at  $x = 0$  to the width  $\sigma_w$ , the frequency chirps from low to high. So when  $n$  is large, the TPPF covers a larger bandwidth range. The central peak width is approximately given by  $\pm \frac{1}{2}x_\pi$ , as illustrated in Fig. 4(b). and used to indicate the contours of the main peaks in Fig. 3

In Fig. 5, we plot  $\sigma_w$  and  $x_\pi$  as the functions of  $z$ , using the parameters in Fig. (2), for fixed ratio  $\rho \equiv \frac{\sigma_2^2}{\sigma_1^2} = 2.56 \times 10^{-6}$ .

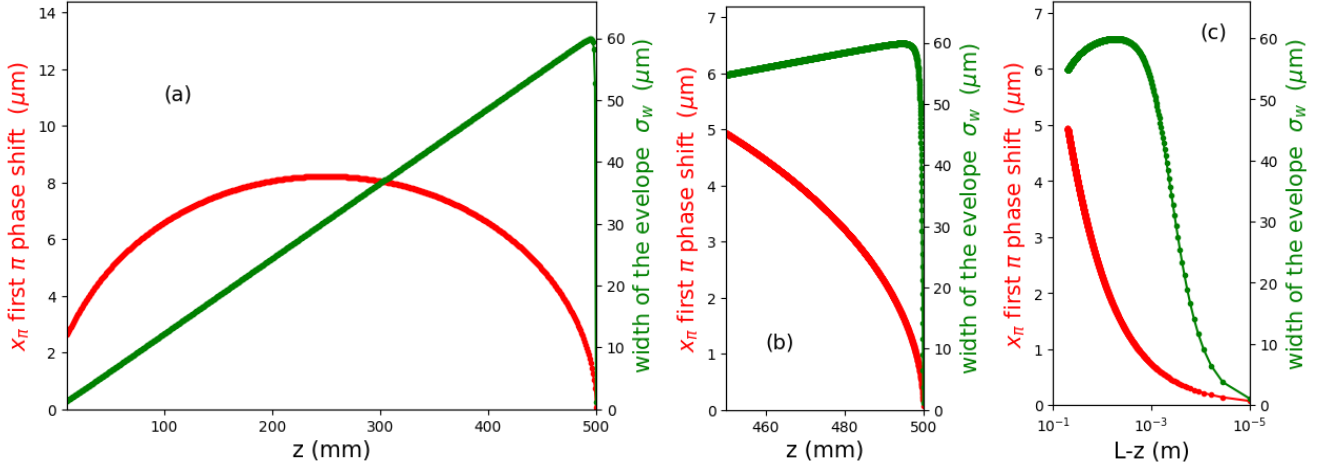


FIG. 5. Width  $x_\pi, \sigma_w$  for the case of  $\lambda = 0.541nm$ ,  $\sigma_1 = 0.5\mu m$ ,  $\sigma_2 = 0.8nm$ ,  $s_1 = 0$ ,  $z_2 = L = 0.5m$ . The maximum width  $x_\pi$  of phase shift  $\pi$  is in the middle point  $z = 0.25m$ . Fig. 5(a): within the valid region of  $x_\pi = \sqrt{\frac{\pi}{\alpha_{\chi i}}}$  for  $0.01m < z < 0.5m - 10\mu m$ . When  $z$  close to 0, paraxial approximation is invalid. When  $z$  is too close to  $0.5m$ ,  $\alpha_{\chi i} = 0$ ,  $x_\pi$  does not exist. Fig. 5(b) :  $\sigma_w = \sqrt{-\frac{1}{2\alpha_{\chi r}}}$  as the function of  $z$  (the green curve) is continuous as it converges to the exit slit near  $z = L = 0.5m$  as shown with details near slit 2 for  $50mm < L - z < 10\mu m$ , as compared with (a). Fig. 5(c): same plot as Fig. 5(b) except  $z$ -axis is replaced by a log scale of  $L - z$ , to see how fast the TPPF converges into the exit slit.

The maximum width of  $x_\pi$  is in the middle between the two slits, while the maximum envelope width is much closer to the slit 2 when  $\sigma_2 \ll \sigma_1$ , so close that we need to use Figs 4(b,c) to see the maximum width  $\sigma_w$  at  $L - z \approx 5mm$ . These two plots demonstrate the rapid convergence of the wave packet into the exit slit again, like we emphasized in Section 2.2 regarding Fig. 2(b).

#### 2.4 Counting number and relation to measurement error bar for a 50-line comb made of 50 pins of 3nm width

Take a point in Fig. 4(c) at  $\sigma_w \approx 40\mu m$  as the pin position, and take a width  $\Delta x = 3nm$ . The probability (we take as the counting rate)  $P_{2b} = 1.86 \times 10^{-5}$ . We first write TPPF in the form of  $\frac{1}{P_{2b}} \frac{\delta P_{2b}}{\delta \chi(x,y,z)} \approx m_{TPPF} \cos(k_x x + \phi)$  to estimate its effect, Eq.(8). The approximate simple formula in Appendix III for numerical  $\alpha_{\chi r}, \alpha_{\chi i}$  in Eq.(10) gives a quick estimation, the peak modulation amplitude of the TPPF is  $m_{TPPF} = \left| \frac{1}{P_{2b}} \frac{\delta P_{2b}}{\delta \chi(x,y,z)} \right|_p = 2 \left| \frac{\sqrt{-\alpha_{\chi}}}{\sqrt{\pi}} \right| \exp(\alpha_{\chi r} \sigma_w^2) \approx 2 \sqrt{\frac{11.6 \times 10^{12} m^{-2}}{\pi}} \times 0.6 = 2.3 \times 10^6 m^{-1}$ . ( $\phi$  is a slowly varying phase). The local phase advance rate of the phase factor of  $\frac{1}{P_{2b}} \frac{\delta P_{2b}}{\delta \chi(x,y,z)}$ , i.e.,  $\exp(i\alpha_{\chi i} x^2)$  gives  $k_x = 2\alpha_{\chi i} x = 2\pi/\lambda_{fringe}$ , with  $\lambda_{fringe} = 6.7nm$  at the TPPF waist  $x = \sigma_w$ . For the opaque pin,  $\Delta\chi = -1$  within the effective blocking width  $\Delta x_{effective} = |\Delta\chi| \Delta x = 3nm$ , Eq.(9) gives the peak to peak counting rate variation  $\left| \frac{\Delta P_{3b}}{P_{3b}} \right|_p \approx 2m_{TPPF} \Delta x_{effective} \approx 0.014$  as the estimation ignoring the width of the pin at the peak position.

The width 3nm is almost half of the period, the more accurate calculation by Eq.(9) gives the contribution of  $\Delta x$  to the final probability  $\left| \frac{\Delta P_{3b}}{P_{3b}} \right|_p \approx 0.0074$ . if we move the pin from a positive peak to a negative, the counting rate will change  $\pm 0.0037$ . The period in Fig. 4(c) is  $T = \lambda_{fringe} \approx 6.7nm$ . If we have 50 pins separated by 6.7nm and move in  $x$  direction, then when pin position from the positive peak moves by 3.35nm, with a  $\pi$ -phase shift, the intensity will change from 18.5% to  $-18.5\%$ . If we further increase the number of pins, the intensity variation will increase. However, if the number of pins is too large, the high attenuation violates the perturbation requirement of the experiment, and the increase will not be linear anymore. If producing a structure 50 pins with a 6.7nm period is difficult, an alternative is to use some well-known structure, such as a crystal, for a calibration of TPPF by orienting it properly to reach the 6.7nm period in the  $x$ -direction. In the example for the X-ray picometer displacement sensor, we consider using a 50-line gold film pattern, as will be discussed in Section 5, which is useful directly for X-ray tomography itself.

To get sufficient accuracy, we use the Poisson distribution formula  $P(k) = \frac{n^k e^{-n}}{k!}$ , its RMS is  $\sqrt{n}$  where  $n$  is the mean rate of events during a fixed interval. Since  $P_{2b} = 1.86 \times 10^{-5}$  for Fig.4, if input photon number is  $N_1 = 2.15 \times 10^9$ , then counting number at slit 2  $N_2 = N_1 P_{2b} = 4 \times 10^4$ , its RMS  $\delta N_2 = \sqrt{N_2} = 200$ , the error of the counting rate  $N_2$  is  $\frac{\delta N_2}{N_2} = \frac{1}{\sqrt{N_2}} = 0.5\%$ . Based on the discussion above, the counting rate change when we move the pins is  $\frac{\Delta P_{2b}(x=\sigma_w)}{P_{2b}} = \frac{\Delta N_2(x=\sigma_w)}{N_2} = 18.5\%$ , and  $\Delta N_2(x = \sigma_w) = N_2 \frac{\Delta P_{2b}(x=\sigma_w)}{P_{2b}} = 7400$ . The signal-to-noise ratio SNR is

$$S_n \equiv \frac{\Delta N_2(x = \sigma_w)}{\delta N_2} = \sqrt{N_2} \frac{\Delta P_{2b}(x = \sigma_w)}{P_{2b}} = \sqrt{N_1 P_{2b}} \frac{\Delta P_{2b}(x = \sigma_w)}{P_{2b}^{(a)}} \quad (11)$$

We find  $S_n = 37$ , the error bar is  $1/S_n = \frac{\delta N_2}{\Delta N_2(x=\sigma_w)} = 2.7\%$ . Increasing the photon number to  $2.15 \times 10^{11}$  will reduce the error to 0.27%.

It is evident that TPPF manifests as a stable, reproducible structure consistent with an objectively existing field with high-resolution fringes, and we will explore it as a tool to probe microscopic structure.

### 3. RELATION BETWEEN TPPF AND RADON TRANSFORM

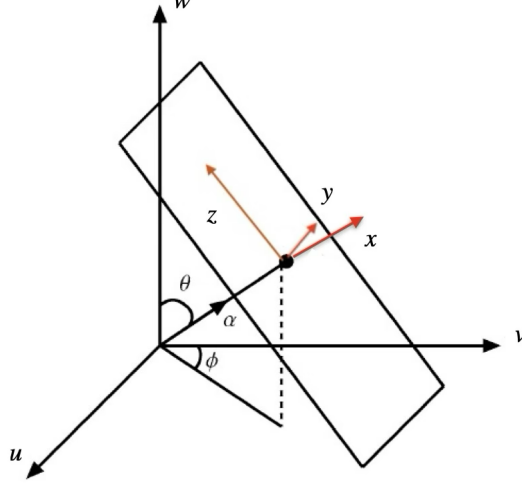
#### 3.1 TPPF is related to the Fourier transform of the Radon transform in 3D tomography

In Eq.(9), we can replace the perturbation of the pin represented by  $\int \Delta\chi(x)dx$  with a perturbation by a sample represented by attenuation  $-\int f(x, y, z)dxdydz$  where  $f(x, y, z)$  is a real function when we only consider attenuation. If there is a phase shift caused by the sample, it is a complex function, but the formulation is the same,

$$\frac{\Delta P_{2b}(s)}{P_{2b}} = \frac{\Delta P_{2b}^{(c)}(s)}{P_{2b}} + c.c. = -\frac{1}{P_{2b}} \int \frac{\delta P_{2b}^{(c)}}{\delta\chi(x, z)} f(x - s, y, z)dxdydz + c.c. \quad (12)$$

Here  $\frac{\delta P_{2b}^{(c)}}{\delta\chi(x, z)}$  is given in Eq.(5). Because the y translational symmetry of Fig. s1 when the slits are long and thin, the functional derivative of  $P_{2b}$  with respect to the perturbation  $\Delta\chi(x, y, z) = f(x, y, z)$  in Eq.(3), i.e. the TPPF function  $\frac{\delta P_{2b}}{\delta\chi(x, z)}$ , is independent of  $y$ , as given by Eq.(8). For an object  $f(x, y, z)$  the size of order of a few  $\mu m$ , the  $z$  dependence of  $\frac{\delta P_{2b}}{\delta\chi(x, z)}$  is also negligible because its only dependence on  $z$  in Eq.(8), is through the  $\alpha_\chi$  dependence on  $\xi = \frac{z}{L}$ . The setup in the example of Fig. 4,  $L = 0.5m$ , and the distance to the slit 2 is  $L - z = 0.5mm$ , so a variation of  $z$  by a few  $\mu m$  compared with the distance of 0.5mm is negligible. In addition, in the following application of Eq.(12) for 3D micro-tomography, we can take this tiny variation into the algorithm without any significant differences because the explicit analytical expression  $\frac{\delta P_{2b}}{\delta\chi(x, z)}$  in Eq.(8) is not needed, we only need the high resolution structure of the TPPF and its Fourier transform. In a practical experiment, its specific value should be measured or calibrated by known samples, there is no need to calculate it accurately. Because the frequency of the waveform  $\frac{\delta P_{2b}}{\delta\chi(x, z)}$  in a small range within a few microns of Fig.4(c) is almost constant like a sinusoidal wave,  $\frac{\Delta P_{2b}(s)}{P_{2b}}$  is approximately a Fourier transform of  $\int f(x, y, z)dxdydz$ . Once  $\frac{\delta P_{2b}}{\delta\chi(x, z)}$  is measured in an experiment,  $\frac{\delta P_{2b}^{(c)}}{\delta\chi(x, z)}$  can be calculated readily by a Hilbert transform, as explained at the end of Section 2.1 (see Appendix AI).

We introduced a translation  $s$  in  $x$  direction representing a scan of the sample in Eq.(12) such that  $\frac{\Delta P_{2b}(s)}{P_{2b}}$  becomes a sum of a convolution between  $\frac{\delta P_{2b}^{(c)}}{\delta\chi(x, z)}$  and  $f(x - s, y, z)$  and its complex conjugate. If the range of  $f$  is a few microns, the range is smaller than the range of TPPF in Fig.4(a). When we change  $s$ , the overlap between  $\frac{\delta P_{2b}^{(c)}}{\delta\chi(x, z)}$



3D projection geometry.

FIG. 6. Relation between the sample reference frame  $(u, v, w)$  and the experiment setup reference frame  $(x, y, z)$

and  $f(x - s, y, z)$  will be in regions of different frequencies because the frequency is chirped in the exponent  $\alpha_\chi x^2$  of  $\frac{\delta P_{2b}^{(c)}}{\delta \chi(x, z)}$  in Eq.(8). When  $s$  increases,  $\frac{\delta P_{2b}^{(c)}}{\delta \chi(x, z)}$  samples higher frequency components in  $f$ . Since  $\frac{\delta P_{2b}^{(c)}}{\delta \chi(x, z)}$  is almost sinusoidal within a few micron range, Eq.(12) is approximately a Fourier transform of  $f$  at a frequency specified by  $s$ . Hence, the scan of  $s$  corresponds to the measurement of the spectrum of  $f$  in the x-direction.  $\frac{\Delta P_{2b}(s)}{P_{2b}}$  is approximately a Fourier transform of  $f(x, y, z)$  in the x-direction.

We now compare Eq.(12) with the Radon transform[5]  $p(s, \vec{\alpha})$  in the 3D tomography for direction  $\vec{\alpha}$ . When we choose the sample reference coordinates  $u, v, w$  such that  $u$  is in  $\vec{\alpha}$  direction, it is the projection of the sample  $f(s, v, w)$  from a plane in the sample perpendicular to  $\vec{\alpha}$  at distance  $s$  from the origin onto a line in the  $\vec{\alpha}$  direction, it converts the 3D density  $f$  into a line density

$$\begin{aligned} p(s, \vec{\alpha}) &= \int \int \int f(\vec{x}) \delta(\vec{x} \cdot \vec{\alpha} - s) d\vec{x} = \int \int \int f(u, v, w) \delta(\vec{x} \cdot \hat{u} - s) dudvdw \\ &= \int \int \int f(u, v, w) \delta(u - s) dudvdw = \int \int f(s, v, w) dv dw \end{aligned}$$

If we choose  $x$ -axis of the TPPF measurement to be in  $\vec{\alpha}$  direction, i.e.,  $\hat{x} = \vec{\alpha}$ , the comparison shows the counting rate  $\frac{\Delta P_{2b}(s)}{P_{2b}}$  is approximately the Fourier transform of the Radon transform mentioned in [5], where  $\int f(x, y, z) dy dz$  is the projection of  $f$  in the  $y, z$  plane onto  $x$ -axis so it converts  $f$  into a line density in  $x$  direction. In Fig. 6, we plot the relation between the sample reference frame and the experiment setup reference frame of Fig. 1(a), varying the Euler angle  $\theta$  and  $\phi$  will change the orientation of the sample while the experimental setup of  $x, y, z$  is fixed. The plot only gives one specific choice of the orientation where  $z$  is pointing to the  $w$ -axis so that the  $w$ -axis is within the  $\{x, z\}$  plane. For this orientation,  $\hat{x} = \vec{\alpha} = (\sin \theta \sin \varphi, \sin \theta \cos \varphi, \cos \theta)$ ,  $\hat{y} = (-\cos \varphi, \sin \varphi, 0)$ ,  $\hat{z} = (-\cos \theta \sin \varphi, -\cos \theta \cos \varphi, \sin \theta)$  in the  $\{u, v, w\}$  coordinate system. However, any rotation of the sample around the  $x$ -axis would not change the  $x$ -line density and gives another choice of the scan orientation of the sample, so our choice here is not unique.

Once the orientation is chosen, the coordinate transform gives the Radon transform function,

$$p(s, \vec{\alpha}) = \int \int f(s, v, w) dv dw = \int \int f(s, y, z) dy dz$$

for the 3D tomography, the starting point is to calculate the Radon transform  $\int \int f(s, y, z) dy dz$ . For this, we rewrite Eq.(12). Since for practical case  $s_1 = s_2$ ,  $x_c = 0$ ,

$$\begin{aligned} g(s) &= \frac{\Delta P_{2b}}{P_{2b}} = \int G^{(c)}(x) f(x - s, y, z) dx dy dz + c.c. \equiv g^{(c)}(s) + g^{(c)*}(s) \\ G^{(c)}(x) &\equiv -\frac{1}{P_{2b}} \frac{\delta P_{2b}^{(c)}}{\delta \chi(x, z)} = -\frac{\sqrt{-\alpha_\chi}}{\sqrt{\pi}} \exp(\alpha_\chi x^2) \\ \hat{g}^{(c)}(\omega) &= \hat{G}^{(c)}(\omega) \hat{f}(\omega) \end{aligned} \quad (13)$$

$g^{(c)}(s)$  here can be calculated from  $g(s)$  by Hilbert transform (See Appendix I) once it is measured, similar to  $G^{(c)}(x)$ . Since the counting rate variation scan  $g^{(c)}(s)$  is the convolution of the complex TPPF  $G^{(c)}(x)$  and the line density  $\int f(x, y, z) dy dz$ , its Fourier transform  $\hat{g}^{(c)}(\omega)$  (FT) is the product of the FT  $\hat{G}^{(c)}(\omega)$  and the FT  $\hat{f}(\omega)$ , i.e., the Fourier transform of Radon transform  $p(s, \vec{\alpha})$ . Let  $\vec{k} = \omega \vec{\alpha}$ ,  $\vec{k} \cdot \vec{x} = \omega x$ , ( $\omega$  is the transverse wavenumber, i.e., we denote the spatial frequency  $k_x = \omega$  in the  $x$  direction),

$$\begin{aligned} \hat{f}(\omega) &= \hat{f}(\omega, \vec{\alpha}) = \hat{f}(\vec{k}) = \int \int \int f(\vec{x}) \exp(-i\vec{k} \cdot \vec{x}) d\vec{x} \\ &= \int dx \exp(-i\omega x) \int \int f(x, y, z) dy dz \\ \hat{f}(\omega) &= \int dx \exp(-i\omega x) p(x, \vec{\alpha}) \end{aligned}$$

$\hat{G}^{(c)}(\omega)$  is the Fourier transform of  $G^{(c)}(x)$ ,

$$\begin{aligned} \hat{G}^{(c)}(\omega) &\equiv \int \exp(-i\omega x) G^{(c)}(x) dx \\ &= \int dx \exp(-i\omega x) \int \int \frac{\sqrt{-\alpha_\chi}}{\sqrt{\pi}} \exp(\alpha_\chi x^2) dy dz \end{aligned} \quad (14)$$

Thus  $\hat{f}(\omega)$  can be calculated as

$$\hat{f}(\omega) = \frac{\hat{g}^{(c)}(\omega)}{\hat{G}^{(c)}(\omega)} \quad (15)$$

In short, structure function  $f(x, y, z)$  can be obtained from  $G(x) = -\frac{1}{P_{2b}} \frac{\delta P_{2b}}{\delta \chi(x, z)}$  measured in an experiment as a calibration, and  $g(t)$  measured by scanning the sample, according to the following steps:

- 1.  $G(x) = -\frac{1}{P_{2b}} \frac{\delta P_{2b}}{\delta \chi(x, z)}$  Hilbert Transform  $\rightarrow$   $G^{(c)}(x)$  Fourier Transform  $\rightarrow$   $\hat{G}^{(c)}(\omega)$ .
- 2. Measure by scan  $g(t)$  Hilbert Transform  $\rightarrow$   $g^{(c)}(x)$  Fourier Transform  $\rightarrow$   $\hat{g}^{(c)}(\omega)$ .
- 3.  $\hat{f}(\omega) = \frac{\hat{g}^{(c)}(\omega)}{\hat{G}^{(c)}(\omega)}$
- 4.  $\hat{f}(\omega)$  Inverse Fourier Transform  $\rightarrow$   $p(x, \vec{\alpha}) = \int \int f(x, y, z) dy dz$

In the following, we find the bandwidth where  $|\hat{G}^{(c)}(\omega)|$  is sufficiently larger than the noise of the system so  $\hat{f}(\omega) = \frac{\hat{g}^{(c)}(\omega)}{\hat{G}^{(c)}(\omega)}$  can be calculated with sufficient precision, which in turn determines the resolution of the 3D tomography.

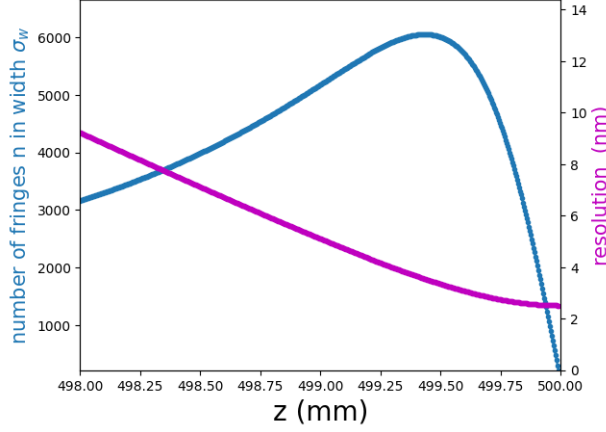


FIG. 7. Number of fringes  $n_f = \frac{\sigma_w^2}{x \frac{\pi}{\pi}}$  in the width  $\sigma_w$  and the resolution vs.  $z$ . For the case of the example in Fig. 4:  $\lambda = 0.541 \text{ nm}$ ,  $\sigma_2 = 0.8 \text{ nm}$ ,  $\sigma_1 = 0.5 \mu\text{m}$ ,  $L = 0.5 \text{ m}$

### 3.2 Bandwidth of $\hat{G}^{(c)}(\omega)$ and the Resolution of the 3D tomograph at the bandwidth

In the application of 3D tomography, the error in the image originates from the measurement of  $g(s)$  and  $G(x)$ . The error is determined by the method of Section 2.4 by photon counting number. We may use  $\hat{G}^{(c)}(\omega)$  calculated from  $G(x)$  in Eq.(13) if the slit 2 is sufficiently narrow and uniform, otherwise, in case the deviation from the idealized slit is significant,  $\hat{G}^{(c)}(\omega)$  should be calculated from the measurement of the counting rate  $G(x)$ . Our discussion on the property of TPPS following the Eq.(12) shows that for each  $s$  in  $\frac{\Delta P_{2b}(s)}{P_{2b}}$  of the equation, there is a corresponding  $\omega$  in the Fourier transform  $\hat{G}^{(c)}(\omega)$  of  $\frac{\delta P_{2b}^{(c)}}{\delta \chi(x,z)}$  that is peaked. This means that when we scan  $s$  from 0 to  $\sigma_w$ , the  $\hat{G}^{(c)}(\omega)$  has a non-zero range as its bandwidth with a low and high frequency limit. Within this bandwidth  $|\hat{G}^{(c)}(\omega)|$  is sufficiently large so that the relative error of  $\frac{\Delta \hat{G}^{(c)}(\omega)}{|\hat{G}^{(c)}(\omega)|}$  is small, and the calculation of  $\hat{f}(\omega)$  from the corresponding  $\hat{g}^{(c)}(\omega)$  is less sensitive to error  $\Delta \hat{G}^{(c)}(\omega)$  in  $\hat{G}^{(c)}(\omega)$ .

In the Fourier transform of the TPPF Eq.(14), because of the discussion in subsection 3.1, we can ignore the  $y$  and  $z$  dependence in the integral when the slits are sufficiently long and narrow. Assuming the slit length is  $\Delta y$  and the sample size in the direction of  $z$  as  $\Delta z$ , we find  $\hat{G}^{(c)}(\omega) = \Delta y \Delta z \exp\left(\frac{\omega^2}{4\alpha_x}\right)$ . The bandwidth  $\sigma_\omega$  is determined as  $\frac{1}{4} \left(\frac{1}{\alpha_x}\right)_r = -\frac{1}{2\sigma_\omega^2}$ , where  $\left(\frac{1}{\alpha_x}\right)_r$  is the real part of  $\frac{1}{\alpha_x}$  (see Appendix III for the approximation of  $\alpha_x$ ). If we cut off  $\hat{G}^{(c)}(\omega)$  at  $\sigma_\omega$ , the resolution limited by this bandwidth is [8]  $\frac{T}{2} = \frac{\pi}{\sigma_\omega} = \pi \sqrt{-\frac{1}{2} \left(\frac{1}{\alpha_x}\right)_r}$ , where  $T$  is the period at the bandwidth  $\sigma_\omega$ . We will first take this as an estimate. At this cutoff,  $\hat{G}^{(c)}(\omega)$  is reduced by a factor  $e^{-\frac{1}{2}} \approx 0.6$ , the noise of 10% would not significantly affect the image reconstruction. For comparison, in the case of the example in Section 2.4 the error bar would be  $\pm 2.7\%$ . Thus, within the bandwidth  $\sigma_\omega$ ,  $\hat{G}^{(c)}(\omega)$  is far from zero, and the solution  $\hat{f}(\omega) = \frac{\hat{g}^{(c)}(\omega)}{\hat{G}^{(c)}(\omega)}$  is stable. If the noise of the measurement is smaller, we may cut off at a higher frequency, and the resolution may be improved if other noise, such as detector noise, is lower.

To minimize the resolution, we observe that  $\alpha_x$  give by Eq.(8) depends on  $\mu \equiv \frac{4\pi\sigma_1^2}{\lambda L}$ ,  $\rho \equiv \frac{\sigma_2^2}{\sigma_1^2}$  and  $z = \xi L$ .

Fig. 7 shows the resolution vs.  $z$  (the magenta curve) for the example in the setup of Fig. 4, together with the number of fringes  $n_f = \frac{\sigma_w^2}{x \frac{\pi}{\pi}}$ . The minimum of the resolution is close to the exit slit at  $L - z = 0.64 \mu\text{m}$ . But we choose  $L - z = 0.5 \text{ mm}$  for the example of Fig.4 because we also need to increase the number of fringes  $n_f$  within the width  $\sigma_w$ . Choosing  $L - z = 0.5 \text{ mm}$  increases the  $s$  scan range in the Radon Fourier transform of Eq.(12). Thus, the scan covers a larger bandwidth from large  $T$  near  $x = 0$  to small period  $T$  at  $x = \sigma_w$ .

To further understand the example of Fig. 5 near slit 2 and the relation of the resolution to  $\sigma_1, \sigma_2, \lambda L$ , and  $z$  more quantitatively, we notice that in this region of a few mm from the exit but not too close to it, we find when  $\mu \ll 1$ ,

$\rho \ll 1$  and  $\xi \approx 1$  (see section 2.3), that is, the slits size is much smaller than the length  $L$  of the setup, and the perturbation sample is much more closer to slit 2 than 1, the parameters satisfy the condition  $|\frac{\alpha_{\chi r}}{\alpha_{\chi i}}| = \frac{\pi\sigma_2^2}{2(1-\xi)\lambda L} \ll 1$  (See Appendix III for the approximation of  $\alpha_\chi$  under this condition, which provides a convenient expression for quick experimental estimates). This implies that the decay rate  $|\alpha_{\chi r}|$  of the TPPF envelope with distance from the axis is much smaller than its oscillation rate  $|\alpha_{\chi i}|$ , provided that  $z$  is sufficiently close to slit 2—but not too close, as an excessively small value of  $1 - \xi$  would invalidate this condition. A comparison with a hard-edged slit 2 shows that, under the same conditions, a hard-edged slit of width  $\sqrt{2}\pi\sigma_2$  is effectively equivalent to a Gaussian slit of width  $\sigma_2$ , with negligible difference in the resulting TPPF.

Thus, under this condition, the number of fringes  $n_f$  is large, and the amplitude of oscillation is still large, even close to the width  $\sigma_w$ . Analysis of Eq.(8) shows when we vary  $z$ , the minimum resolution is  $\frac{T_0}{2} = \pi\sigma_2$ , achieved when  $\zeta \equiv 1 - \xi - \frac{\rho}{\rho+2} = 0$ , under the assumed condition  $\alpha_{\chi r}^2 \ll \alpha_{\chi i}^2$ . The analysis shows the assumption is self-consistent, i.e., at the minimum found, the assumption is satisfied. The resolution satisfies a formula similar to the formula for the Rayleigh range as

$$\left(\frac{T}{2}\right)^2 = \left(\frac{T_0}{2}\right)^2 \left(1 + \left(\frac{\Delta z}{L_R}\right)^2\right).$$

Here,  $\Delta z = L\zeta = L\left(1 - \xi - \frac{\rho}{\rho+2}\right)$  is the distance from the position of the minimum resolution where  $\zeta = 0$ . According to this,  $\frac{T}{2}$  increases by a factor  $\sqrt{2}$  at  $\Delta z = L_R = \sqrt{\frac{L}{2}}$  from the minimum. In the example of Fig. 5, the minimum is at  $L - z = 0.64\mu m$ ,  $L_R = \sqrt{\frac{L}{2}} = \sqrt{\frac{2.56 \times 10^{-6}}{2}} \times 0.5m = 0.56mm$ . Thus, when we choose  $L - z = 0.5mm$  in the example, the resolution is only slightly larger than the minimum, while the number of fringes  $n_f = 6011$ , as shown in Fig. 4.

Thus, the resolution at the minimum as a function of  $z$  is the slit size  $\pi\sigma_2 = 0.8\pi nm \approx 2.5nm$ . As we choose  $L - z = 0.5mm$ , the resolution is about 3nm. This is the resolution when we choose the cutoff at  $\sigma_w$ . If we lower the shot noise by increasing the counting number, and if the detector noise can be neglected, we may increase the cutoff frequency to  $2\sigma_w$ , and hence further improve the resolution, as we will explore later.

Notice that the resolution discussed here is mainly determined by the slit 2 width, the cut-off bandwidth of  $\omega$ , and the noise, and it is insensitive to the choice of the photon wavelength  $\lambda$ .

### 3.3 Relation of the cut-off frequency to the resolution, the sample size, and the scan range

The quadratic dependence  $\phi_x \equiv \alpha_\chi x^2$  in Eq.(13), leads to the phase advance rate, i.e., the local frequency  $k_x = \omega(x) = \frac{d\phi_x}{dx} = 2\alpha_{\chi i}x$ , which is linearly dependent on  $x$  and hence also linear in  $s$  in Eq.(12). Near the narrow slit  $\sigma_2$  applying the approximation of  $\alpha_\chi$  using the approximation formula in Appendix III, we find  $2\alpha_{\chi i}\sigma_w \approx \sigma_\omega$  at the position of the width of TPPF, i.e., when  $x = \sigma_w$ , the frequency  $k_x$  is about equal to the bandwidth of  $|\hat{G}^{(c)}(\omega)|$  defined as  $\sigma_\omega$  where it drops to  $\exp(-\frac{1}{2}) \approx 0.6$  of the peak at  $\omega = 0$ . In Fig.4(a) at  $x = \sigma_w$ ,  $\frac{\delta P_{2b}}{\delta\chi(x_p, z)}$  also drops to 0.6 of its peak value, while  $\frac{\Delta P_{2b}(x)}{P_{2b}}$  drops to 0.32 of its peak, not 0.6 because the pin width  $\Delta\chi = 3nm$  is almost half of the period  $T = 6.7nm$  at  $x = \sigma_w$ .

Hence, a cutoff of  $\hat{G}^{(c)}(\omega)$  at  $\sigma_\omega$  is equivalent to a cutoff of the scan of  $s$  in the Radon Fourier transform at  $\sigma_w$ , like the example in Figs. 2 and 3. Indeed, the example has a period  $T = 2(\sqrt{6012}x_\pi - \sqrt{6011}x_\pi) = 2 \times 3.35nm = 6.7nm$ . And hence if we scan  $s$  from  $x = 0$  to  $\sigma_w$ , or within  $\{-\sigma_w < x < \sigma_w\}$ , the upper-limit bandwidth will be  $\sigma_\omega$ , and the resolution will be  $\frac{T}{2} = \frac{\lambda_{fringe}}{2} = 3.35nm$ , and the minimum  $|\hat{G}^{(c)}(\omega)|$  will be  $\exp(-0.5) = 0.6$  of  $|\hat{G}^{(c)}(\omega = 0)|$ .

If we choose the cutoff at  $x = 2\sigma_w$ , the spatial frequency  $\omega(x = 2\sigma_w) = 2\alpha_{\chi i}\sigma_w$  is doubled. The TPPF amplitude (see Sec.2.4) becomes  $m_{TPPF} \equiv \left|\frac{1}{P_{2b}} \frac{\delta P_{2b}}{\delta\chi(x, y, z)}\right|_p = 2\left|\frac{\sqrt{-\alpha_\chi}}{\sqrt{\pi}}\right| \exp(4\alpha_{\chi r}\sigma_w^2)$ , since  $\exp(\alpha_{\chi r}\sigma_w^2) = \exp(-0.5) = 0.6$ ,

the amplitude drops by the factor  $\exp(4\alpha_{\chi r}\sigma_w^2) / \exp(\alpha_{\chi r}\sigma_w^2) = \exp(-1.5) = 0.223$ , the required incident photon number would increase by a factor  $0.223^{-2} \approx 20$  to recover the same signal-noise ratio as for the  $\frac{\lambda_{fringe}}{2} = 3.35nm$  resolution, according the analysis in Section 2.4, while the resolution will reach  $\frac{T}{2} = \frac{\lambda_{fringe}}{2} = 1.68nm$ .

The line density as a function of  $\vec{\alpha}$  (i.e., the Euler angle scan over  $\theta, \phi$ ) is used to reconstruct the 3D tomography using standard reconstruction algorithms—for example, the algebraic reconstruction techniques described in Ref. [10]. This establishes a relation between the TPPF measurement and its application in X-ray micro-tomography. Here, we do not elaborate on the reconstruction procedures, which will require extensive discussion with X-ray tomography experts. Instead, we will first need to address the practical feasibility of the 2 nm width slit and the experiment to replace the high displacement sensitivity of the 50-line comb made of 50 pins of 3nm width with a more preferred practical gold film pattern of 50-line comb. Thus, before we can extensively explore the X-ray micro-tomography, we were able to establish the feasibility of a picometer X-ray displacement sensor in this paper as a first step in the exploration of the application of TPPF in tomography by a practical double-triple slit cascade addressed in the next section.

#### 4. CASCADED DOUBLE AND TRIPLE SLIT FOR NANOMETER RESOLUTION USING EXISTING TECHNOLOGY

To achieve 3.3nm resolution, we need to use a hard edge slit 2 of width  $\sqrt{2\pi}\sigma_2 \approx 2nm$  ( $\sigma_2 \approx 0.8nm$ ) as shown in the last section. The publication from CFN at BNL[11, 12] indicates the feasibility of the required slit. An example of 2nm wide, 1cm long 150nm thick slit of gold is given by ref[13].

The thickness of the slit is one parameter relevant to the aspect ratio of the slit and the difficulties of the manufacture of the slit. The possible achievable thickness of the slit to achieve sufficient attenuation still needs to be investigated because it will determine the attenuation outside the slit. We will explore the possibility of using the 150nm slit [13] in the following cascaded triple slit. For a simple numerical test, we first assume a cascaded double slit and assume it is possible to achieve 400nm thickness for a 2nm gold slit. According to the Mass attenuation coefficient table[14], we have for  $x = 400nm$ , the attenuation is  $\exp(-(\mu/\rho)\rho x) = \exp(-(2389cm^2/g) * (19.3g/cm^3) * (40x10^{-6}cm)) \approx 0.158$ . To further attenuate outside the slit, we need a cascaded double slit with the second slit 10nm wide and  $2\mu m$  thick slit. The aspect ratio would be the same because both the width and the thickness of the slit are increased by a factor 5. Then  $\exp(-(\mu/\rho)\rho x) = \exp(-(2389cm^2/g) * (19.3g/cm^3) * (200x10^{-6}cm)) \approx 1 \times 10^{-4}$ , and outside the cascaded double slit the full attenuation is  $0.158 \times 1 \times 10^{-4} = 1.58 \times 10^{-5}$ . The geometry of the cascaded double slit is shown in Fig. 8(a), and its transmission in Fig. 8(b).

##### 4.1 2nm Cascaded Double slit transmission profile and its relation to counting rate $P_{2b}$ and the rate change $\frac{\Delta P_{2b}(x=\sigma_w)}{P_{2b}}$ during Radon Fourier transform scan at the TPPF width

The 10nm wide  $2\mu m$  slit  $b$ , illustrated as the lower white rectangle in Fig.8(b) has transmission  $c_b = 0.158$ . The transmission of the 2nm wide 400nm thick slit  $a$  is illustrated as the white rectangle at the top of Fig.8(b) with transmission of  $c_a = 0.842$  so that  $f_2^2(x_2 = 0) = c_a + c_b = 1$ . The transmission of the cascaded double slit is the sum of the transmissions of the two slits  $f_2^2(x_2) = c_a f_2^2(x_2, \sigma_a) + c_b f_2^2(x_2, \sigma_b)$  in Eq.(7), where  $f_2^2(x_2, \sigma_a) = \exp(-\frac{x_2^2}{2\sigma_a^2})$  is the transmission of a  $\sqrt{2\pi}\sigma_a = 2nm$  slit with  $f_2^2(0, \sigma_a) = 1$  in its Gaussian approximation. Its complex TPPF is  $\frac{\delta P_{2b}^{(c)(a)}(\sigma_2 \rightarrow \sigma_a)}{\delta \chi(x, z)}$ , and is given by Eq.(8) with  $\sigma_2$  replaced by  $\sigma_a$ . Similarly, the TPPF of the 10nm slit is  $\frac{\delta P_{2b}^{(c)(b)}(\sigma_2 \rightarrow \sigma_b)}{\delta \chi(x, z)}$ . Because  $\frac{\delta P_{2b}^{(c)}}{\delta \chi(x, z)}$  in Eq.(6) is linear in  $f_2^2(x_2)$ , we have  $\frac{\delta P_{2b}^{(c)}}{\delta \chi(x, z)} = c_a \frac{\delta P_{2b}^{(c)(a)}(\sigma_2 \rightarrow \sigma_a)}{\delta \chi(x, z)} + c_b \frac{\delta P_{2b}^{(c)(b)}(\sigma_2 \rightarrow \sigma_b)}{\delta \chi(x, z)}$  for the cascaded double slit. Hence the convolution TPPF function, essential for the 3D tomography in Eq.(13), is  $G^{(c)}(x) = -\frac{1}{P_{2b}} \frac{\delta P_{2b}^{(c)}}{\delta \chi(x, z)} = c_a \frac{P_{2b}^{(a)}}{P_{2b}} G_a^{(c)}(x) + c_b \frac{P_{2b}^{(b)}}{P_{2b}} G_b^{(c)}(x)$ . Here,  $G_a^{(c)}(x)$  and  $G_b^{(c)}(x)$  are the convolution TPPF functions for single slit  $a$  and  $b$ , respectively. And  $P_{2b}^{(a)}, P_{2b}^{(b)}$  are their respective detection rates.

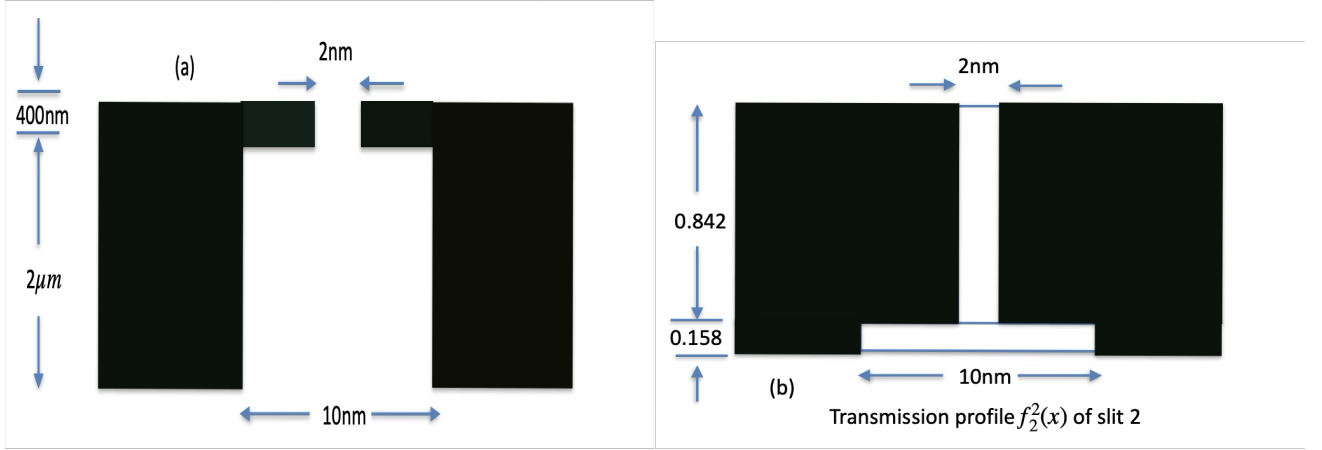


FIG. 8. Schematic illustration (**not to scale**) of (a) the 2nm and 10nm slits combination. (b) The transmission profile of  $f_2^2(x)$  is the sum of the profiles of two slits. Both plot are not to scale; relative lengths are distorted to highlight structural features of the slits and to clarify the function's behavior.

For a narrow slit size  $\sqrt{2\pi}\sigma_a = 2nm$  and  $\sqrt{2\pi}\sigma_b = 10nm$ ,  $\rho = \frac{\sigma_a^2}{\sigma_b^2} \rightarrow 0$ , the detection rate in Eq.(8)  $P_{2b}(s_2, \sigma_2 = \sigma \rightarrow 0) \rightarrow \sigma \sqrt{\frac{2k\mu}{L(\mu^2+1)}} \exp\left(-\frac{k\mu}{L(\mu^2+1)}s_2^2\right) \equiv \sigma \frac{\partial P_{2b}^{(0)}}{\partial \sigma}$  is a good approximation with negligible errors. Hence for the cascaded double slit,  $P_{2b} = c_a P_{2b}^{(a)} + c_b P_{2b}^{(b)} \approx (c_a \sigma_a + c_b \sigma_b) \frac{\partial P_{2b}^{(0)}}{\partial \sigma}$ . When we substitute this,  $P_{2b}^{(a)} = \sigma_a \frac{\partial P_{2b}^{(0)}}{\partial \sigma}$ , and  $P_{2b}^{(b)} = \sigma_b \frac{\partial P_{2b}^{(0)}}{\partial \sigma}$  into the  $G^{(c)}(x)$  derived above, we find  $G^{(c)}(x) = C_a G_a^{(c)}(x) + C_b G_b^{(c)}(x)$ , and where we denote  $C_a \equiv \frac{c_a \sigma_a}{c_a \sigma_a + c_b \sigma_b}$ ,  $C_b \equiv \frac{c_b \sigma_b}{c_a \sigma_a + c_b \sigma_b}$ . Hence, its Fourier transform  $\hat{G}^{(c)}(\omega) = C_a \hat{G}_a^{(c)}(\omega) + C_b \hat{G}_b^{(c)}(\omega)$  in Eq.(14) for the cascaded double slit. In the same way, we also find  $P_{2b} = \frac{c_a}{C_a} P_{2b}^{(a)}$  to express the cascaded double slit parameter in terms of the single slit.

Since the slit  $a$  is narrower than the slit  $b$ , the bandwidths  $\sigma_\omega^{(a)} > \sigma_\omega^{(b)}$ . As we pointed out in Section 3.3, the frequency at  $x = \sigma_w^{(a)}$  is about equal to the bandwidth of  $|\hat{G}_a^{(c)}(\omega)|$ , i.e.  $\sigma_\omega^{(a)}$ . In addition, the TPPF width  $\sigma_w^{(a)} > \sigma_w^{(b)}$  too. At  $x = \sigma_w^{(a)} > \sigma_w^{(b)}$ , the frequency of  $G_b^{(c)}(x)$  is beyond its bandwidth  $\sigma_\omega^{(b)}$ , thus  $|G_b^{(c)}(x = \sigma_w^{(a)})|$  is exponentially reduced and is negligibly small compared with  $|G_a^{(c)}(x = \sigma_w^{(a)})|$ . Hence for the Radon Fourier transform scan at the width  $s = \sigma_w^{(a)}$ ,  $G^{(c)}(x = \sigma_w^{(a)}) = C_a G_a^{(c)}(x = \sigma_w^{(a)})$ , in simple term this means at the beam waist of slit a, the TPPF is only determined by slit a, the contribution from slit b is negligible. Similarly, at the bandwidth  $\omega = \sigma_\omega^{(a)}$ ,  $\hat{G}^{(c)}(\omega = \sigma_\omega^{(a)}) = C_a \hat{G}_a^{(c)}(\omega = \sigma_\omega^{(a)})$ . In particular, for the Radon Fourier transform in the  $s$  scan, the main signal crucial for the resolution is measured at  $s = \sigma_w^{(a)}$ , where  $\frac{\Delta P_{2b}}{P_{2b}} = C_a \frac{\Delta P_{2b}^{(a)}}{P_{2b}^{(a)}}$ , according to Eq.(13). Thus, the achievable resolution is determined by the amplitude of TPPF at  $\sigma_w^{(a)}$ .

$\frac{\Delta P_{2b}}{P_{2b}} = C_a \frac{\Delta P_{2b}^{(a)}}{P_{2b}^{(a)}}$  and  $P_{2b} = \frac{c_a}{C_a} P_{2b}^{(a)}$  expressed the photon counting number and its variation of the cascaded double slit in terms of a single idealized slit.

This derivation shows that the cascaded double slit acts as a spatial frequency filter, the 2nm slit allows critically important high frequency components to reach the beam waist at  $x = \sigma_w$  while cutting off the lower frequency components. The 10nm slit allows the low frequency component near the center to pass through to the detector while suppressing them to low intensity outside the 10nm slit, and hence lowers the low frequency components, which if not cutoff, would increase the total detected photon number and the shot noise, and degrade the resolution mainly determined by high frequency components.

## 4.2 The counting number and its relation to the measurement signal-to-noise ratio at the width $\sigma_w^{(a)}$ of TPPF of resolution 3.3nm

For a single slit of width  $\sigma_a$  and with idealized thickness, in Section 2.4 we find the signal-to-noise ratio (SNR) is  $S_{na} \equiv \frac{\Delta N_{2a}(x=\sigma_w^{(a)})}{\delta N_{2a}} = 37$ . To derive the SNR for the double slit in the following, we denote the parameters of the idealized single slit by subscript  $a$  to distinguish them from the parameters for the cascaded double slit.

For a cascaded double slit instead of a single slit  $a$ , apply the result of the last section  $P_{2b} = \frac{c_a}{C_a} P_{2b}^{(a)}$  and  $\frac{\Delta P_{2b}(x=\sigma_w^{(a)})}{P_{2b}} \approx C_a \frac{\Delta P_{2b}^{(a)}(x=\sigma_w^{(a)})}{P_{2b}^{(a)}}$  to Eq.(11), we find  $S_n = \frac{\Delta N_2(x=\sigma_w^{(a)})}{\delta N_2} = \sqrt{N_1 P_{2b}} \frac{\Delta P_{2b}(x=\sigma_w^{(a)})}{P_{2b}} = \sqrt{N_1} \frac{c_a}{C_a} P_{2b}^{(a)} C_a \frac{\Delta P_{2b}^{(a)}(x=\sigma_w^{(a)})}{P_{2b}^{(a)}}$ . If we keep  $N_1 = N_{1a}$ , then  $S_n = \sqrt{c_a C_a} S_{na}$ . Since  $c_a C_a < 1$ , the SNR for the cascaded double is smaller than the idealized single slit. If we choose  $N_1 = \frac{1}{c_a C_a} N_{1a}$ , then the SNR is recovered to  $S_n = S_{na}$ . As a result  $N_2$  increases by a factor  $\frac{1}{C_a^2}$ , while  $\delta N_2$  and  $\Delta N_2(x = \sigma_w^{(a)})$  both increase by a factor  $\frac{1}{C_a}$  compared with the idealized single slit  $a$ , to keep  $\Delta N_2(x = \sigma_w^{(a)})/\delta N_2$  unchanged.

For the parameters in Fig.4 at 2.29keV, with the cascaded double slit in Fig. 8 ( $c_a = 0.842$ ,  $C_a = \frac{c_a \sqrt{2\pi\sigma_a}}{c_a \sqrt{2\pi\sigma_a} + c_b \sqrt{2\pi\sigma_b}} = \frac{0.842 \times 2nm}{0.842 \times 2nm + 0.8158 \times 10nm} = 0.516$ ),  $\sqrt{c_a C_a} = 0.66$ . Thus, SNR becomes  $0.66 \times 37 \approx 24$ . If the input photon number remains as  $2.15 \times 10^9$ . To recover to  $SNR = 37$  we need to increase by a factor  $1/(c_a C_a) = 2.27$  to  $4.9 \times 10^9$ .

### 4.3 Assessment of 3.3 nm Resolution and SNR=37 when the requirement on the slit thickness is reduced from 400nm to 150nm for a cascaded triple slit

If we prefer using the existing example in ref.[13] to produce a 2nm wide 150nm thick slit instead of the 400nm thick example in the cascaded double slit, we consider using the 150nm slit combined with another two slits aligned together. The extension of the discussion of the cascaded double slit in Sections 4.1 and 4.2 to a cascaded triple slit is straightforward. We consider a 2nm wide 150nm slit, a 4nm wide 300nm slit aligned with a 10nm wide  $2\mu m$  slit. Following the same way as 4.1, the first slit attenuates to 50%,  $c_a = 1 - 0.5 = 0.5$ , the second slit, further from 0.5 attenuates to  $c_c = 0.25 * 0.5 = 0.125$ , so  $c_b = 0.5 - 0.125 = 0.375$ . Then, outside slit b, the transmission drops from 0.125 to nearly zero. Thus, the transmission drops from 1 to 0.5 to 0.125 to zero in 3 steps as  $x_2$  moves away from the center. Hence, the cascaded triple slit function is  $f_2^2(x_2) = c_a f_2^2(x_2, \sigma_a) + c_b f_2^2(x_2, \sigma_b) + c_c f_2^2(x_2, \sigma_c)$ . Again, we have  $P_{2b} = \frac{c_a}{C_a} P_{2b}^{(a)}$ . Since the TPPF width and the bandwidth of the slit  $b$  and  $c$  are smaller than  $a$ , we can choose cut off at  $x = \sigma_w^{(a)}$  to reach the bandwidth given by the slit  $a$ , and we have  $\frac{\Delta P_{2b}(x=\sigma_w^{(a)})}{P_{2b}} \approx C_a \frac{\Delta P_{2b}^{(a)}(x=\sigma_w^{(a)})}{P_{2b}^{(a)}}$  again except now  $C_a = \frac{c_a \sigma_a}{c_a \sigma_a + c_b \sigma_b + c_c \sigma_c} = 0.267$ , and,  $\frac{1}{c_a C_a} = 7.5$ .

Now following the same steps as 4.2, the error bar increases from 2.7% to 7.4% by the factor  $\sqrt{\frac{1}{c_a C_a}} = 2.74$  when the cascaded triple slit is used. To recover the error bar due to the shot noise back to 2.7%, we need to increase the photon number at slit 1 from  $N_1 = 2.1 \times 10^9$  to  $16 \times 10^9$  by the factor  $\frac{1}{c_a C_a} = 7.5$ . Therefore, given a realistic noise floor 2.7%, the 3.3nm resolution is likely achievable if the sample has enough Fourier strength at that frequency. If other sources of noise is much less than 2.7%, and if the signal in the sample is less, it might be necessary to increase the photon number at slit 1. On the other hand, if the signal is larger than 2.7%, the photon number required may be reduced.

## 5. PICOMETER X-RAY DISPLACEMENT SENSING VIA TWO-POINT PROPAGATION FIELD

With the cascaded double-triple slit calculation ready, our next step to develop TPPF-based tomography is to analyze the feasibility of replacing the 50-line comb made of 50 pins of 3nm width, preferably and more practically, by a single

$\sim 15 - 25 \text{ nm}$ -thick gold film patterned with 50 lines of  $6.7 \text{ nm}$  period, operated at  $x \approx 40 \mu\text{m}$ . The discussion on the cascaded double-triple slit in Section 4, indicated the feasibility of such a comb as a sample using the technology in refs.[11–13]. We apply the formula developed in sections 2,3,4 to provide the first step of testing the TPPF and its connection with tomography to show that the gold film pattern can be used as a lensless picometer x-ray displacement sensor.

**Detection rate variation of the gold film pattern.** We assume a modulation depth of  $10 \text{ nm}$ , the modulated attenuation depth estimated using the gold  $\mu/\rho$  given in Section 4 is  $m_{\text{gold}} = 0.023$ , Since the gold film sample width  $\Delta x = 330 \text{ nm} \ll \sigma_w$ , the gold film attenuation is  $\Delta\chi(x - x_p) = m_{\text{gold}} \cos(kx - kx_p)$ , and  $\frac{1}{P_{2b}} \frac{\delta P_{2b}}{\delta\chi(x,y,z)} \approx m_{\text{TPPF}} \cos(kx + \phi)$ , given as  $m_{\text{TPPF}} = 2.3 \times 10^6 \text{ m}^{-1}$  in Section 2.4, we have  $\frac{\Delta P_{2b}}{P_{2b}} \approx \frac{1}{P_{2b}} \frac{\delta P_{2b}}{\delta\chi(x,y,z)} \Delta\chi(x - x_p) \Delta x \approx \frac{1}{2} m_{\text{TPPF}} m_{\text{gold}} \cos(kx_p - \phi) \Delta x$ , ignoring the term with a fast oscillating phase  $2kx$ . Thus, when we move the gold film  $x_p$  by  $3.35 \text{ nm}$ , the peak to peak variation is  $|\frac{\Delta P_{2b}}{P_{2b}}|_p = m_{\text{TPPF}} m_{\text{gold}} \Delta x \approx 0.0175$ .

**The incident photon number  $N_{1a}$  required to achieve 15 pm sensitivity for an idealized slit 2 with photon counting  $N_{2a}$ .** The detection probability is  $P_{2b} = 1.86 \times 10^{-5}$  in our example (see Fig. 4). Assume the photon counting number  $N_{2a} = 4 \times 10^6$  at the detector behind the slit 2, the RMS shot noise is  $\delta N_{2a} = \sqrt{N_{2a}} = 2000$ , when we move the gold film pattern  $x_p$ , the photon counting variation is  $\Delta N_{2a} = |\frac{\Delta P_{2b}(s)}{P_{2b}}|_p N_{2a} = 0.0175 \times 4 \times 10^6 = 7 \times 10^4$ . Thus the signal noise ratio is  $\frac{\Delta N_{2a}}{\delta N_{2a}} = |\frac{\Delta P_{2b}(s)}{P_{2b}}|_p \sqrt{N_{2a}} = 0.0175 \times \sqrt{4 \times 10^6} = 35$ .

From the discussion above, the photon counting signal is  $\Delta N_{2a} = N_{2a} |\frac{\Delta P_{2b}}{P_{2b}}|_p \cos(kx_p - \phi_1)$ . Then shot-noise-limited displacement sensitivity follows directly from Poisson statistics of the detected photons, the sensitivity is  $\delta x_p = \frac{\delta N_{2a}}{k N_{2a} |\frac{\Delta P_{2b}}{P_{2b}}|_p} = \frac{\lambda_{\text{fringe}}}{2\pi \sqrt{N_{2a}} |\frac{\Delta P_{2b}}{P_{2b}}|_p} = \frac{6.7 \text{ nm}}{2\pi \sqrt{4 \times 10^6} \times 0.0175} = 15 \text{ pm}$ .

The incident photon number at the entrance slit 1 when the slit 2 is idealized is  $N_{1a} = \frac{N_{2a}}{P_{2b}} = \frac{4 \times 10^6}{1.86 \times 10^{-5}} \approx 2.15 \times 10^{11}$ . Then for a possible cascaded double-triple slit, we calculate for the following 4 options.

**5.1 Cascaded Double slit with first slit 2nm wide 400nm thick.** We apply the analysis of the cascaded double slit in Sections 4.2 and 4.3. The example of ALD gold on SiN membranes in reference [13] is a  $2 \text{ nm}$  wide,  $150 \text{ nm}$  thick, and  $2 \text{ cm}$  long slit. We first consider an option of a possible  $\sqrt{2\pi}\sigma_a = 2 \text{ nm}$  wide  $400 \text{ nm}$  depth first slit followed by a  $\sqrt{2\pi}\sigma_b = 10 \text{ nm}$  wide  $2 \mu\text{m}$  depth slit. The first slit suppresses the intensity to  $c_b = 0.158$  right before the second slit b, then the latter further suppresses the intensity to  $\ll 10^{-4}$  and can be ignored. Thus, the slit a contributes to the transmission by  $c_a = 1 - c_b = 0.842$ .

The TPPF for the  $2 \text{ nm}$  wide slit given Eq.(8) as a function of  $x$ , is dominated by a simple factor  $\exp(\alpha_{\chi_r} x^2) = \exp(\alpha_{\chi_r} x^2) \exp(i\alpha_{\chi_i} x^2)$ , where  $\alpha_{\chi} = \alpha_{\chi_r} + i\alpha_{\chi_i}$  is a complex valued parameter with  $|\alpha_{\chi_i}| \gg |\alpha_{\chi_r}|$  and  $\alpha_{\chi_r} < 0$  (see Sec. 2.3). The factor  $\exp(i\alpha_{\chi_i} x^2)$  results in a chirp of high spatial frequency  $k_x = 2\alpha_{\chi_i} x$  linearly increasing with  $x$ , while the amplitude of TPPF slowly drops according to a factor  $\exp(\alpha_{\chi_r} x^2)$ . At the beam waist  $x = \sigma_w \approx 40 \mu\text{m}$ ,  $\exp(\alpha_{\chi_r} x^2) = \exp(-1/2) \approx 0.6$ , and  $k_{\sigma_w} = 2\pi/\lambda_{\text{fringe}}$  with  $\lambda_{\text{fringe}} = 6.7 \text{ nm}$ . The width of the TPPF for the  $10 \text{ nm}$  slit b has much smaller angular spread, i.e., its width in  $x$  is smaller and its contribution dominates the region of  $x \ll \sigma_w = 40 \mu\text{m}$ , while its contribution at  $x = \sigma_w \approx 40 \mu\text{m}$  is negligible. Thus, TPPF near  $x = 40 \mu\text{m}$  is dominated by the TPPF of slit a, so it remains as if there is only slit a. The combined effect of the cascaded double slit is that TPPF for low spatial frequency  $k_x$  increased while at  $x = 40 \mu\text{m}$  remains the same. This gives the quantitative analysis of the cascaded double slit in Section 4.1 a qualitative interpretation.

The analysis in Section 4.1 shows when the cascaded double slit replace the single idealized slit a, because the low spatial frequency component increased, the shot noise increased, the signal noise ratio becomes  $\text{SNR} = \frac{\Delta N_{2a}}{\delta N_{2a}} = \sqrt{c_a C_a} \frac{\Delta N_{2a}}{\delta N_{2a}}$ , where  $C_a \equiv \frac{c_a \sigma_a}{c_a \sigma_a + c_b \sigma_b} = \frac{0.842 \times 2 \text{ nm}}{0.842 \times 2 \text{ nm} + 0.158 \times 10 \text{ nm}} = 0.516$ .  $\frac{\Delta N_{2a}}{\delta N_{2a}}$  is the SNR when there is only one idealized slit a. Thus, for the cascaded double slit  $\text{SNR} = \sqrt{0.842 \times 0.516} \times 35 = 23$ .

The derivation in 4.2 shows, to recover the SNR back to 35, thus also recover the position sensitivity back to  $15 \text{ pm}$ , we need to increase the incident photon number to  $N_1 = \frac{1}{c_a C_a} N_{1a} = \frac{1}{0.842 \times 0.516} \times 2.15 \times 10^{11} = 4.9 \times 10^{11}$ .

**5.2 Cascaded Triple slit with first slit 2nm wide, 150nm thick.** Assume we apply the technique based on the existing example in [13], we generalize the cascaded double slit to a cascaded triple slit. We consider a cascaded triple slit TPPF for  $2.29 \text{ keV}$  case ( $0.541 \text{ nm}$  case), (a)  $2 \text{ nm}$  wide,  $150 \text{ nm}$  thick, (b)  $4 \text{ nm}$  wide,  $300 \text{ nm}$  thick, (c)  $10 \text{ nm}$

wide,  $2\mu\text{m}$  thick. The performance calculation using the formula in 4.1 is almost the same as the cascaded double slit. Using the same gold  $\mu/\rho$  and the formula in 4.2, the first slit a attenuates to 50%,  $c_b = 1 - 0.5 = 0.5$ , the second slit b, further from 0.5 attenuates to  $0.25 * 0.5 = 0.125$  before the slit c, so  $c_b = 0.5 - 0.125 = 0.375$ . Then, outside slit c, the transmission drops from 0.125 to nearly zero ( $\sim 1.2 \times 10^{-5}$ ). Thus, we find with  $c_a = 0.5$ ,  $\sqrt{2\pi}\sigma_a = 2\text{nm}$ ,  $c_b = 0.375$ ,  $\sqrt{2\pi}\sigma_b = 4\text{nm}$ ,  $c_c = 0.125$ ,  $\sqrt{2\pi}\sigma_c = 10\text{nm}$ .  $C_a \equiv \frac{c_a\sigma_a}{c_a\sigma_a + c_b\sigma_b + c_c\sigma_c} = 0.267$ ,  $c_a C_a = 0.133$ . To recover the increased signal noise ratio back to 35, and 15pm sensitivity, we need to increase the incident photon number to  $N_1 = \frac{N_{1a}}{c_a C_a} = \frac{2.15 \times 10^{11}}{0.133} = 1.6 \times 10^{12}$ .

**5.3 Cascaded Triple slit with first slit 4nm wide, 300nm thick.** If we would like to avoid using the most advanced technology as prescribed in [13], a more robust 4 nm first slit gives identical performance at  $\sim 2.8 \times 10^{12}$  photons but uses the same aspect ratio for the slit. We consider a cascaded triple slit consisting of 3 slits: (a) 4nm wide, 300nm thick, (b) 10nm wide, 750nm thick, (c) 20nm wide,  $1.5\mu\text{m}$  thick. For  $\sqrt{2\pi}\sigma_2 = 4\text{nm}$ , we find  $\alpha_{\chi_i}$  (See Appendix III) remains the same, so at  $x \approx 40\mu\text{m}$ , the fringe spacing  $\lambda_{fringe} = 6.7\text{nm}$  remains the same, while  $\alpha_{\chi_r}$  increased by a factor 2.68, thus the amplitude factor  $\exp(\alpha_{\chi_r} x^2)$  drops from  $\exp(-1/2) = 0.6$  to  $\exp(-1/2 \times 2.68) = 0.261$ . Thus, the amplitude drops by a factor  $\frac{0.6}{0.261} = 2.3$ . To achieve the same precision, we need to increase the photon number by a factor  $2.3^2 \approx 5.3$ . For the cascaded triplet now with the first 4nm wide slit a has  $c_a C_a = 0.749 \times 0.536 = 0.40$ . Thus, we need to increase the incident photon number to  $N_1 = \frac{N_{1a}}{c_a C_a} = \frac{5.3 \times 2.15 \times 10^{11}}{0.4} = 2.8 \times 10^{12}$  for the same precision of 15pm.

**5.4 Cascaded Triple slit with first slit 2nm wide, 150nm thick, and the gold film pattern at  $x = 80\mu\text{m}$  to achieve sensitivity at 7.5pm.** To improve the sensitivity to displacement further down to 7.5 pm we consider still using the cascaded triple slit with a first 2 nm wide 150nm thick slit. We need to double the position of the gold film pattern from  $40\mu\text{m}$  to  $x = 80\mu\text{m}$ . Since the only change is  $x$  in the dominating factor  $\exp(i\alpha_{\chi_i} x^2)$  of the TPPF, the frequency  $k_x = 2\alpha_{\chi_i} x$  becomes  $k_x = 2\pi/\lambda_{fringe}$  with fringe spacing halved to  $\lambda_{fringe} = 3.35\text{nm}$ , but the amplitude factor drops from  $\exp(\alpha_{\chi_r} \sigma_w^2) = \exp(-1/2) \approx 0.6$  in section 3.1 to  $\exp(\alpha_{\chi_r} 4\sigma_w^2) = \exp(-2) \approx 0.135$  by a ratio  $0.6/0.135 = 4.4$ . Thus, to recover to the same signal noise ratio, we need to increase the incident photon number by the ratio squared to  $N_1 = \frac{4.4^2 N_{1a}}{c_a C_a} = \frac{4.4^2 \times 2.15 \times 10^{11}}{0.133} \approx 3.1 \times 10^{13}$ .

In short, we considered 4 possible options for the slit 2: (1) A cascaded double slit with first 2 nm wide 400nm thick slit need incident photon number  $N_1 = 4.9 \times 10^{11}$  to reach sensitivity of 15pm for the idealized single 2nm slit a. (2) A cascaded double slit with first 2 nm wide 150nm thick slit:  $N_1 = 1.6 \times 10^{12}$ , 15pm sensitivity. (3) A cascaded triple slit with a first 4 nm wide 300nm thick slit:  $N_1 = 2.8 \times 10^{12}$ , 15pm sensitivity. (4) A cascaded double slit with a first 2 nm wide 150nm thick slit:  $N_1 = 3.1 \times 10^{13}$  for 7.5pm sensitivity.

We note that, in our example, the displacement sensitivity is  $\delta x \approx 15\text{pm}$ , while the photon's momentum spread is bounded by  $\delta p \leq h/\lambda$  (with  $\lambda = 0.541\text{nm}$ ). This yields  $\delta x \delta p < 15\text{pm} \times h/0.541\text{nm} \approx 0.026h$ . Compared to the Heisenberg uncertainty relation  $\Delta x \Delta p \geq h/4\pi \approx 0.08h$ , we have  $\delta x \delta p \lesssim (1/3)(\Delta x \Delta p)$ . Since  $\delta x$  represents the relative movement of the macroscopic gold film pattern with respect to the TPPF structure—rather than a direct measurement of the photon's position—this result is consistent with the uncertainty principle and poses no violation.

### 5.5 The Broadening from Finite X-ray beam bandwidth $\frac{\Delta E}{E}$

The calculations assume a monochromatic beam. For finite bandwidth, by Eq.(10), the TPPF phase  $\phi = \alpha_{\chi_i} x^2 \approx \frac{\pi x^2}{\lambda L(1-\epsilon)}$  shifts relatively as  $\frac{\delta \phi}{\phi} = -\frac{\delta \lambda}{\lambda}$ . To compensate this shift (maintain constant phase at fixed  $x$ ), a displacement  $\delta x = \frac{x}{2} \frac{\delta \lambda}{\lambda}$  is required. At the beam waist  $x = \sigma_w \approx 40\mu\text{m}$  and  $\frac{\delta \lambda}{\lambda} = 10^{-5}$ , this yields  $\delta x \approx 200\text{pm}$ . Optionally, to match the shot-noise-limited sensitivity to this broadening (rather than 15 pm), the required incident photons  $N_{1a} \approx 2.15 \times 10^{11}$  are reduced by a factor  $\left(\frac{200\text{pm}}{15\text{pm}}\right)^2 \approx 178$ , to  $N_{1a} \approx 1.2 \times 10^9$ . Correspondingly the flux required in the 4 options above, is also reduced by the same factor. Practical grating monochromators achieve  $\Delta E/E \approx 10^{-5}$ ; ultra-high-resolution optics can approach lower values.

## 6 PROSPECTIVE FLUX REDUCTION VIA CENTRAL SPATIAL-FREQUENCY FILTERING AND MULTIPLE DETECTOR SLIT OPTION AND THEIR INFLUENCE ON THE DEVELOPMENT OF LENSLESS X-RAY PICOMETER AND RADON FOURIER TRANSFORM BASED X-RAY MICRO-TOMOGRAPHY

The TPPF at  $|x| \approx 40 \mu\text{m}$  has a high spatial frequency ( $\lambda_{fringe} \approx 6.7\text{nm}$ ). Photons propagating near  $x \approx 0$  contribute negligibly to the sinusoidal signal at  $6.7\text{nm}$  but dominate the total detected counting number  $N_2$  and thus the shot noise. A micron-scale opaque blocker placed centrally  $0.4\text{mm}$  before slit 2 is expected to suppress this useless background by  $>90\%$  while leaving the signal-carrying high-frequency component nearly untouched. A preliminary estimate suggests the required  $N_1$  could drop below  $10^{10}$ – $10^{11}$  photons for  $15 \mu\text{m}$  sensitivity — a  $>10$ – $100\times$  improvement in speed and dose. Full wave-optical calculation is in progress.

Another, potentially far more powerful flux-reduction strategy is to use a two-dimensional array of many detection slits displaced from the optical axis ( $s_2 \neq 0$  in Fig. 1). Because the TPPF fringes at different off-axis positions are laterally shifted, their intensity modulations add incoherently when summed: the total signal scales linearly with the number of slits  $N_{slit}$ , while shot noise scales only as  $\sqrt{N_{slit}}$ . A moderate 2-D array of  $N_{slit} = 10^3$  detection channels — readily achievable in the near term by fabricating arrays of triple-slit cascades with  $20$ – $50 \mu\text{m}$  pitch over a few-millimetre detector area — is estimated to reduce the required incident fluence by an additional two orders of magnitude. Larger custom arrays ( $N_{slit} \gtrsim 10^4$ ), which would also eliminate mechanical scanning and enable instantaneous picometer readout with extremely low radiation dose for biological samples, appear feasible with continuing advances in nanofabricated multi-slit technology.

So far for simplicity, we only consider a single slit 2 at  $x = s_2 = 0$ , while Eq.(8) the analytical expression of TPPF already gives the option of  $s_2 \neq 0$ . Depends on the technology available for the separate slit 2 at another location, such as  $s_2 = 1\mu\text{m}$ , we may consider a slit array to simultaneously record the counting rate for other sample positions and hence for other spatial frequencies without increasing the incident photons. This option requires revising the TPPF-Radon Fourier transform relation Eq.(13), to increase a variable  $s$  in  $g(s), G^{(c)}(x)$  to  $g(s, s_2), G^{(c)}(x, s_2)$ , with a remark that  $s$  here is the position of the sample relative to  $x$ , while  $s_2$  is the position of slit 2. In principle, this would not change the formulation of TPPF-Radon Fourier transform relation, except it increases the matrix dimension in the reconstruction program, also extends the calibration of TPPF from  $s_2 = 0$ , to a calibration of TPPF for various  $s_2$ . However, this does not increase the time the calibration takes because all these various  $s_2$  calibration can be done simultaneously with  $s_2 = 0$ . A single photon detection can at most be in one of these slits 2, and for the multiple slits 2, each can only record the photons statistics at its position with the corresponding spatial frequency and phase, however their accumulation of data is simultaneous, so the total statistics of the slit array will be increased proportionally by a factor of 100 or more to significantly reduce the required scan points in the Radon scan if it is possible to minimize the spacing of the slit to the order of  $1\mu\text{m}$ . If the array of slits 2 also includes different  $y$  position of slits 2, then even the number of Radon scans in  $y$ -direction can be reduced too. Hence, their impact on reducing the flux and radiation damage will be expected to be significant.

Another remark is the gold film attenuation introduced  $\Delta\chi(x - x_p) = m_{gold} \cos(kx - kx_p)$ , where  $m_{gold}$  can be replaced in tomography by the Fourier expansion coefficient  $m_{sample}$  at a specified wavelength  $\lambda_{fringe}$ , and the formula can be used to estimate the required incident photon number to achieve a desired resolution, just as our analysis in Section 5 for the x-ray picometer sensor.

Both possibility can provide significant flux reduction for the x-ray picometer sensor, and for further improve of the lensless x-ray-tomography, in particular, it will reduce the flux requirement and hence reduce the radiation damage to the sample due to those photons reaching the sample, which is only a small fraction of the incident photon number. This reduction may have a significant impact on the application of tomography of biomolecular samples.

## 7. RELATION TO QUANTUM MEASUREMENT DURING THE FREE SPACE PROPAGATION BETWEEN THE SOURCE AND DETECTOR SLIT

The TPPF concept originates from a perturbative study of single-particle propagation and measurement [2]. The consideration and interpretation of the following questions about this measurement problem led to the TPPF concept. This then turns to the X-ray picometer displacement sensor and the connection to tomography.

We first discuss the system in Fig. 1 with  $\Delta\chi(x) = 0$  because the following fundamental question in quantum mechanics. The wave function of a single particle starting from the entrance slit becomes wide-spread before it strikes the screen with the exit slit, as shown in Fig 1(b). Most times, it is not detected, but there is a fixed probability that it is detected. And in the instant of the detection, the wave function collapses into the slit with energy  $h\nu$ . We understand there is no contradiction with relativity here because the wave function is only a probability amplitude, after the detection our knowledge changes from a probability distribution of the particle to a point. However, there is a question about whether and how the associated energy distribution of  $h\nu$  also collapses. Whatever happens, the energy  $h\nu$  becomes concentrated in the detector when detected. Experimental investigation is difficult because any intermediate measurement between the source and detection slits either collapses the wave function or substantially alters it. Even in a weak measurement, for example, as discussed in an overview[15], the wave function is significantly altered. In the example [16], it is caused by magnets, in the case of [17, 18], it is caused by lenses.

To seek an answer for this question, in Fig. 1(a), we study the effect of a perturbation  $\Delta\chi(x)$  on the counting rate  $P_{2b} = \int_{-\infty}^{\infty} dx_2 |\psi_{2b}(x_2)|^2$ , and calculate the ratio of the counting rate change over the perturbation. As the perturbation approaches zero, the ratio  $\frac{\Delta P_{2b}}{\Delta\chi(x,z)}$  becomes the functional derivative  $\frac{\delta P_{2b}}{\delta\chi(x,z)}$  of the counting rate over the perturbation  $\Delta\chi(x)$ . This perturbative function is independent of perturbation. It is a real-valued function containing high-resolution phase information, determined solely by the two-slit geometry in our 2D study as we show in the Fig. 2. It can be measured with high precision and reproducibility, it uniquely characterizes the individual event of a particle propagating between the two slits. Unlike a probability amplitude, it manifests as a stable, reproducible structure that we interpret as consistent with an objectively existing field, which we define as the two-point propagation field (TPPF). The TPPF does not correspond to a probability distribution. While the wave function describes an ensemble of possible detection outcomes, the TPPF characterizes the process underlying a single detection — a realization selected according to the Born rule.

While these interpretative aspects remain speculative, experimental validation of the TPPF through picometer sensing could provide empirical insights into such foundational questions

## 8. CONCLUSION

The analysis based on the TPPF and the cascaded triple slit estimation provides, (1) An experimental test basis for TPPF as a detailed wavefunction collapse process where fine fringes, without lens or focusing, continuously converge to the 2 nm slit and confirm that TPPF turns the wave function into a measurable observable with 15 pm displacement precision, while a measurement of the wave function absolute square, as a probability density, lost the phase information in the propagation. (2) A direct feasibility study of a practical tool to stabilize the displacement between the x-ray beam and the sample, as one of the main goals of this work. The tool itself can be very useful for tomography applications, because the motion between the x-ray beam and the sample of order of 4 nm is one of the limitations of tomography resolution[1]. And (3) provide a direct calibration of TPPF function  $\frac{1}{P_{2b}} \frac{\delta P_{2b}^{(c)}}{\delta\chi(x,z)}$  in Eq.(12) for various spatial wavelengths obtained by various orientations of the gold film pattern. As we discussed in Section 3.1, this function is the basis of the Radon Fourier transform to be used for the tomography, and we should use this experimentally calibrated function rather than the theoretical function of Eq. (8) because this would remove the systematic error between the experimental setup and the theoretical model. (4). It also bridges between the TPPF experimental confirmation and nanometer x-ray micro-tomography, and provides a basis for a more detailed study in this direction, from the Radon scan to the photon number required to achieve the resolution. (5) The example here is not optimized for tomography because the parameters such as  $\lambda, L - z, \sigma_1, \sigma_2, x$  have large room for variation, depending on sample mass attenuation coefficients, sample's attenuation Fourier expansion coefficients, damage threshold, prior knowledge for reconstruction of tomography, etc. This justifies engaging in discussions with X-ray tomography experts to develop simulations that test the new lensless method and determine the best achievable resolution. For example, we can reduce the incident photon number at the expense of lower precision. Here we provide a simple analytical tool to help with the assessment.

Hence, the picometer X-ray displacement Sensing via TPPF, in addition to its direct application in X-ray tomography, is also a stepping stone for the exploration of its application in a new method in X-ray tomography based on Radon Fourier transform. This becomes clearer when we consider the ongoing study discussed in Section 6 to significantly reduce the photon flux.

The TPPF bears analogy to Green's functions or propagators, offering a real-valued, measurable correlate to complex amplitudes, potentially extensible to high-energy contexts.

We thank Dr. T. Shaftan, and Dr. V. Smaluk for their discussion and suggestions on the manuscript.

## APPENDIX I HILBERT TRANSFORM

For a real function with Fourier expansion  $u(t) = \sum_{-n}^n a_n e^{i\omega_n t}$ , its Hilbert transform is  $H(u)(t) = \sum_{-n}^n b_n e^{i\omega_n t}$  such that for terms with  $\omega_n > 0$ ,  $b_n = -ic_n$ , for terms with  $\omega_n < 0$ ,  $b_n = ic_n$ , for terms with  $\omega_n = 0$ ,  $b_n = 0$ . Then  $f(t) = u(t) + iH(u)(t)$  is an analytical function. The real part of  $f(t)$  is  $u(t)$ , its imaginary part is  $H(u)(t)$ . Thus, once we have  $u(t)$  we can calculate its amplitude and phase from  $f(t)$  using The Hilbert transform.

## APPENDIX II ANALYTIC TPPF $\frac{\delta P_{2b}^{(c)}}{\delta \chi(x,z)}$ EXPRESSED BY $\alpha_\chi$ AND $P_{2b}$

The complex TPPF  $\frac{\delta P_{2b}^{(c)}}{\delta \chi(x,z)}$  in Eq.(6) is a triple Gaussian integral over three variables  $x_1, x_2, x'_1$ , each of which can be integrated by the formula

$$\int dx \exp(ax^2 + bx + c) = \left(\frac{\pi}{-a}\right)^{\frac{1}{2}} \exp\left(-\frac{b^2}{4a} + c\right) = \exp\left(-\frac{b^2}{4a} + c + \ln\left(\frac{\pi}{-a}\right)^{\frac{1}{2}}\right), \quad (16)$$

The integral over  $x'_1$  result is expressed by the parameters  $\mu, \rho, \xi$  defined before Eq.(8) in Section 2.2 in terms of the basic parameters in the setup in Fig.1:  $\sigma_1, \sigma_2, \lambda, k, L$ , and  $z$ ,

$$\frac{\delta P_{2b}^{(c)}}{\delta \chi(x,z)} = \left(\frac{1}{2\pi^3 \sigma_1^2 (1-\xi)\xi \left(1 - \frac{i}{\mu}\right)}\right)^{\frac{1}{2}} \left(\frac{ik}{2L}\right) \int_{-\infty}^{\infty} dx_2 \int_{-\infty}^{\infty} dx_1 \exp\left[\frac{ik}{2L} f(x_1, x_2)\right] \quad (17)$$

$$f(x_1, x_2) = A_1 \left(x_1 - \frac{B_1}{A_1}\right)^2 + A_2 \left(x_2 - \frac{B_2}{A_2}\right)^2 + C$$

where  $A_1, B_1, A_2, B_2, C$  are expressed in term of the basic parameters,  $A_1, A_2$  are independent of  $x, s_1, s_2$  the variable indicated in Fig.1, while  $B_1, B_2$  are linear in  $x, s_1, s_2$ ,  $C$  is a quadratic polynomial of  $x, s_1, s_2$ .

The integral over  $x_1, x_2$  in Eq.(17) then carried out as a Gaussian integral by Eq.(16), the result is

$$\begin{aligned}
\frac{\delta P_{2b}^{(c)}}{\delta \chi(x, y, z)} &= \left( \frac{1}{2\pi\sigma_1^2(1-\xi)\xi \left(1 - \frac{i}{\mu}\right) A_1 A_2} \right)^{\frac{1}{2}} \exp \left[ \frac{ik}{2L} a(x-b)^2 + \frac{ik}{2L} D \right] \\
A_1 &= \frac{1}{\xi} + \frac{i}{\mu}, A_2 = \frac{1}{1-\xi} + \frac{2i}{\rho\mu} - 1 + \frac{1}{1 - \frac{i}{\mu}}, \\
a &= \left( \frac{1}{(1-\xi)} + \frac{1}{\xi} \right) - \left( \frac{1}{A_1 \xi^2} + \frac{1}{A_2 (1-\xi)^2} \right) \\
b &= \frac{1}{a} \left( \frac{b_1}{A_1 \xi} + \frac{b_2}{A_2 (1-\xi)} \right) \\
b_1 &= \frac{is_1}{\mu}, b_2 = \frac{2is_2}{\rho\mu} + \frac{i s_1}{1 - \frac{i}{\mu}} \\
D &= C(x=0) - ab^2 \\
C(x=0) &= \frac{2i}{\rho\mu} (s_2)^2 + \frac{2i}{\mu} s_1^2 - \frac{1}{\mu^2 \left(1 - \frac{i}{\mu}\right)} s_1^2 - \left( \frac{\left(\frac{is_1}{\mu}\right)^2}{A_1} + \frac{\left(\frac{2is_2}{\rho\mu} + \frac{i s_1}{1 - \frac{i}{\mu}}\right)^2}{A_2} \right)
\end{aligned} \tag{18}$$

Since  $P_{2b} = \frac{1}{2} \int_{-\infty}^{\infty} dx \frac{\delta P_{2b}}{\delta \chi(x, z)} = \int_{-\infty}^{\infty} dx \frac{\delta P_{2b}^{(c)}}{\delta \chi(x, z)}$  is independent of  $z$ , we use this to simplify the calculation of  $\frac{\delta P_{2b}^{(c)}}{\delta \chi(x, y, z)}$ , and find

$$P_{2b} = \int dx \frac{\delta P_{2b}^{(c)}}{\delta \chi(x, y, z)} = \left( \frac{1}{-2\sigma_1^2(1-\xi)\xi \left(1 - \frac{i}{\mu}\right) \frac{ik}{2L} a A_1 A_2} \right)^{\frac{1}{2}} \exp \left[ \frac{ik}{2L} D \right]$$

Now compare this with  $P_{2b} = \sqrt{\frac{\mu^2 \rho}{\mu^2 + \rho\mu^2 + 1}} \exp \left( -\frac{1}{2\sigma_1^2} \frac{\mu^2}{\mu^2 + 1 + \mu^2 \rho} (s_1 - s_2)^2 \right)$  derived as Eq.(10) of refs.[2], we can simplify the two complicated expressions. Compared with the coefficient and the exponent of  $P_{2b}$ , we find the following relation,

$$(1-\xi)\xi \left(1 - \frac{i}{\mu}\right) \frac{ik}{2L} a A_1 A_2 = \frac{\mu^2 + \rho\mu^2 + 1}{-2\sigma_1^2 \mu^2 \rho}. \tag{19}$$

Applying this relation, the complex TPPF in Eq.(18) is simplified as an exponential function expressed by a parameter  $\alpha_\chi$  that determines the peak, width and spatial frequency distribution of TPPF,

$$\begin{aligned}
\frac{\delta P_{2b}^{(c)}}{\delta \chi(x, z)} &= P_{2b} \sqrt{\frac{-\frac{ik}{2L} a}{\pi}} \exp \left[ \frac{ik}{2L} a(x-b)^2 \right] = P_{2b} \sqrt{\frac{-\alpha_\chi}{\pi}} \exp [\alpha_\chi (x - x_c)^2] \\
\alpha_\chi &= -\frac{i\mu (\mu^2 + \rho\mu^2 + 1)}{2\sigma_1^2 (-i\mu + \xi) (2(\xi - 1) (\mu i + 1) + \mu (i\xi - \mu) \rho)}
\end{aligned}$$

Now with  $2k\sigma_1^2 = \mu L$ , use the relation Eq.(19), we find  $x_c$ ,

$$\begin{aligned}
x_c &= \frac{c_{S1}s_1 + c_{S2}s_2}{\mu^2 + \rho\mu^2 + 1} \\
c_{S1} &\equiv \rho\mu^2 - (i\mu + 1)(\xi - 1), c_{S2} \equiv (\mu - i)(\mu + i\xi)
\end{aligned} \tag{20}$$

### APPENDIX III APPROXIMATION OF $\alpha_\chi, P_{2b}$ NEAR NARROW SLIT $\sigma_2$

The formula Eq.(8) for  $\alpha_\chi$  is not complicated. But the order of magnitude estimation of  $\alpha_{\chi r}, \alpha_{\chi i}, \text{Re}\left(\frac{1}{\alpha_\chi}\right)$ , and  $\text{Im}\left(\frac{1}{\alpha_\chi}\right)$  in its small slit size limit  $\mu = \frac{4\pi\sigma_1^2}{\lambda L} \ll 1$ ,  $\rho = \frac{\sigma_2^2}{\sigma_1^2} \ll 1$  is simpler, in particular when close to slit 2 when , as in the 3D tomography study:

$$\begin{aligned}
\alpha_{\chi i} &\approx -\frac{\mu}{4\sigma_1^2} \frac{1}{\xi(\xi - 1)} \approx \frac{\pi}{\lambda L} \frac{1}{1 - \xi} \\
\alpha_{\chi r} &\approx -\frac{\mu^2}{4\sigma_1^2} \frac{(\rho\xi^2 + 2(\xi - 1)^2)}{2\xi^2(\xi - 1)^2} \approx -\left(\frac{\pi}{\lambda L} 2\sigma_1\right)^2 \left(1 + \frac{\rho}{2(\xi - 1)^2}\right)
\end{aligned}$$

$$\begin{aligned}
\text{Re}\left(\frac{1}{\alpha_\chi}\right) &= -2\sigma_1^2 \frac{(\rho(\mu^2 + \xi^2) + 2(\xi - 1)^2)}{(\mu^2 + \rho\mu^2 + 1)} \approx -2\sigma_1^2 \rho = -2\sigma_2^2 \\
\text{Im}\left(\frac{1}{\alpha_\chi}\right) &\approx 4\sigma_1^2 \frac{(\xi - 1)}{\mu} (-\mu^2 - \rho\mu^2 + 1) \approx -\frac{\lambda L}{\pi} (1 - \xi)(1 - \mu^2) \\
P_{2b} &\approx \frac{4\pi\sigma_1\sigma_2}{\lambda L} \exp\left(-\frac{\mu^2}{2\sigma_1^2}(s_1 - s_2)^2\right)
\end{aligned}$$

- 
- [1] Aidukas T, Phillips NW, Diaz A, Poghosyan E, Müller E, Levi AFJ, et al., “High-performance 4-nm-resolution X-ray tomography using burst ptychography,” *Nature*. 2024; 632(8023): 81-88.
- [2] Li Hua Yu, “Perturbative study of wave function evolution from source to detection of a single particle and the measurement”, <http://arxiv.org/abs/2412.15409> (2024)
- [3] Flannery, B. P., Deckman, H. W., & D’Amico, K. L. (1987). *Three-Dimensional X-Ray Microtomography*. Science, 237(4821), 1439-1443.
- [4] J Pathol Actions Search in PubMed Search in NLM Catalog Add to Search . 2019 Aug;189(8):1608-1620. doi: 10.1016/j.ajpath.2019.05.004. Epub 2019 May 22. X-ray Micro-Computed Tomography for Nondestructive Three-Dimensional (3D) X-ray Histology Orestis L Katsamenis 1, Michael Olding 2, Jane A Warner 3, David S Chatelet 2, Mark G Jones 4, Giacomo Sgalla 5, Bennie Smit 6, Oliver J Larkin 6, Ian Haig 6, Luca Richeldi 5, Ian Sinclair 7, Peter M Lackie 8, Philipp Schneider 9.
- [5] Amir Averbuch and Yoel Shkolnisky, *Appl. Comput. Harmon. Anal.* 15 (2003) 33–69
- [6] K. A. Milton, *The Casimir Effect: Physical Manifestations of Zero-Point Energy*, World Scientific (2001).
- [7] [https://en.wikipedia.org/wiki/Hilbert\\_transform](https://en.wikipedia.org/wiki/Hilbert_transform)
- [8] Goodman, J. W., *Introduction to Fourier Optics*, 4th ed., Roberts & Company Publishers, 2017.
- [9]
- [10] Algebraic Reconstruction Algorithms, Purdue University, [https://engineering.purdue.edu/~malcolm/pct/CTI\\_Ch07.pdf](https://engineering.purdue.edu/~malcolm/pct/CTI_Ch07.pdf)
- [11] Vitor R. Manfrinato†Aaron Stein†Lihua Zhang†Chang-Yong Nam†OrcidKevin G. Yager†Eric A. Stach\*†OrcidCharles T. Black\*, “Aberration-Corrected Electron Beam Lithography at the One Nanometer Length Scale “, *Nano Letters Vol 17/Issue 8 Article, Expand Letter* April 18, 2017

- [12] Fernando E. Camino<sup>1</sup>, Vitor R. Manfrinato<sup>1</sup>, Aaron Stein<sup>1</sup>, Lihua Zhang<sup>1</sup>, Ming Lu<sup>1</sup>, Eric A. Stach<sup>1</sup>, Charles T. Black<sup>1</sup>, JoVE Journal Engineering, “Single-Digit Nanometer Electron-Beam Lithography with an Aberration-Corrected Scanning Transmission Electron Microscope” Published: September 14, 2018 doi: 10.3791/58272, <https://www.jove.com/t/58272/single-digit-nanometer-electron-beam-lithography-with-an-aberration>
- [13] Xiaoshu Chen<sup>1\*</sup>, Hyeong-Ryeol Park<sup>1\*</sup>, Nathan C. Lindquist<sup>2</sup>, Jonah Shaver<sup>1</sup>, Matthew Pelton<sup>3</sup> & Sang-Hyun Oh<sup>1</sup>, Squeezing Millimeter Waves through a Single, Nanometer-wide, Centimeter-long Slit, SCIENTIFIC REPORTS | 4 : 6722 | DOI: 10.1038/srep06722,
- [14] <https://physics.nist.gov/PhysRefData/XrayMassCoef/ElemTab/z79.html>
- [15] [https://en.wikipedia.org/wiki/Weak\\_measurement](https://en.wikipedia.org/wiki/Weak_measurement)
- [16] Yakir Aharonov, David Z. Albert, and Lev Vaidman, VOLUME 60, NUMBER 14 PHYSICAL REVIEW LETTERS How the Result of a Measurement of a Component of the Spin of a Spin- 2 Particle Can Turn Out to be 100.
- [17] Jeff S. Lundeen<sup>1</sup>, Brandon Sutherland<sup>1</sup>, Aabid Patel<sup>1</sup>, Corey Stewart<sup>1</sup> & Charles Bamber<sup>1</sup>,”Direct measurement of the quantum wavefunction”, 1 8 8 | N A T U R E | V O L 4 7 4 | 9 J U N E 2 0 1 1
- [18] Sacha Kocsis,<sup>1,2\*</sup> Boris Braverman,<sup>1\*</sup> Sylvain Ravets,<sup>3\*</sup> Martin J. Stevens,<sup>4</sup> Richard P. Mirin,<sup>4</sup> L. Krister Shalm,<sup>1,5</sup> Aephraim M. Steinberg<sup>1†</sup>, “bserving the Average Trajectories of Single Photons in a Two-Slit Interferometer”, 3 JUNE 2011 VOL 332 SCIENCE,O